applied sciences

MDPI

Article

Mechanical Characteristics Analysis and Structural Optimization of Key Component of Self-Moving Temporary Support

Shuhui Ding [1,2], Jindong Bai [1], Jingliang Han [1], Haixia Wang [1,*] and Fai Ma [2]

[1] College of Mechanical and Electronic Engineering, Shandong University of Science and Technology, Qingdao 266590, China
[2] Department of Mechanical Engineering, University of California, Berkeley, CA 94709, USA
* Correspondence: wanghx@sdust.edu.cn

Abstract: In order to prevent a roof fall accident of a coal mine roadway mining face, temporary support must be provided before the permanent support of the roadway. At present, the commonly used forepoling bar support has poor reliability and low efficiency, and other machine-mounted or self-moving temporary supports are also difficult to use widely due to the complex geological conditions and limited working space at the heading face. On the basis of the mechanical characteristics analysis and numerical simulation of the wall rock support system, we propose a temporary support scheme that can adapt to the uneven roof of the roadway and the complex geological conditions on site, and that can ensure the cooperative operation of multiple equipment on site. A self-moving temporary support (SmTS) is designed, and its mechanical characteristics are analyzed to meet the mechanical requirements of the wall rock support system on the mining face. The multiobjective optimization of the main beam structure based on response surface methodology (RSM) is carried out to eliminate the design redundancy on the premise of meeting the support requirements of the main beam. Our research provides a novel method and corresponding equipment for the temporary support of a mining face. Applications of the proposed approach in the 7900 mining area of a mine proves the effectiveness of the method and equipment.

Keywords: roadway temporary support; self-moving temporary support (SmTS); wall rock support system; multiobjective optimization design; response surface methodology (RSM)

check for updates

Citation: Ding, S.; Bai, J.; Han, J.; Wang, H.; Ma, F. Mechanical Characteristics Analysis and Structural Optimization of Key Component of Self-Moving Temporary Support. *Appl. Sci.* **2022**, *12*, 10745. https://doi.org/10.3390/app122110745

Academic Editor: Abílio Manuel Pinho de Jesus

Received: 27 September 2022
Accepted: 21 October 2022
Published: 24 October 2022

Publisher's Note: MDPI stays neutral with regard to jurisdictional claims in published maps and institutional affiliations.

Copyright: © 2022 by the authors. Licensee MDPI, Basel, Switzerland. This article is an open access article distributed under the terms and conditions of the Creative Commons Attribution (CC BY) license (https://creativecommons.org/licenses/by/4.0/).

1. Introduction

At present, bolt support is widely used as permanent support during the tunneling of fully mechanized roadway in coal mines, and temporary support must be provided to prevent the roof caving of the tunneling face before the bolt support. At present, a number of front probe beams are generally suspended on the roof bolts along the roadway as temporary supports. The front probe beams extend forward to the empty roof area to protect the roof and prevent personal injury and death caused by roof fall. With the above support method, the initial support force cannot be applied to the roof, the support range is limited, it is impossible to work in parallel with the roadheader [1], the reliability is poor [2], the support efficiency is low [3,4], and the safety hazard is large [5]. To solve this problem, scholars and enterprises have proposed various types of machine-mounted or self-moving temporary supports, but due to their own structure, they have not been widely used [6].

The geological conditions of a tunneling roadway are complex, the roof is uneven, there are many equipment and personnel in the roadway, and the space is narrow [7]. Based on the above situation, we propose a self-moving temporary support method based on the analysis of the mechanical characteristics of the wall rock of the roadway and build a numerical simulation method for the mechanical characteristics of the support and a multiobjective optimization method for the key components based on it.

The existing research similar to our study mainly focuses on the integrated equipment such as machine-mounted temporary support and mining–tunnelling–anchoring integrated machine. These devices are highly automated, but because they are integrated with other equipment, they have high space requirements. At the same time, due to the simple support structure, they cannot adapt to the actual working conditions of complex geological conditions and an uneven roof. This paper plans to solve the problem of the temporary support of roadways with complex geological conditions. On the basis of a mechanical analysis of the wall rock support system and a numerical simulation of the support pressure, a self-moving temporary support (SmTS) suitable for uneven roadway roof is constructed, and its mechanical characteristics are analyzed. A multiobjective optimization method for key components based on response surface methodology (RSM) is constructed to optimize and analyze the key components of the support. The application of our research can realize the efficient and reliable temporary support of a tunneling roadway and provide a temporary support method in the process of coal mine roadway tunneling, which can solve the problems of low efficiency, poor reliability, and large potential safety hazards of the temporary support of a tunneling roadway.

The remainder of the paper is organized as follows. Section 2 reviews the literature relating to the temporary support of roadway and its relevant analysis and optimization. In Section 3, the mechanical analysis and numerical simulation of the wall rock support system of the tunneling roadway is introduced. A self-moving temporary support method is constructed in Section 4. In Section 5, the multiobjective optimization of the main beam is carried out, followed by a conclusion in Section 6.

2. Literature Review

In order to realize the temporary support work in the process of roadway excavation, scholars have carried out a lot of research in the field of temporary support design, support analysis, and optimization.

2.1. Temporary Support Equipment for Roadway

Temporary support equipment for a roadway refers to the equipment used to temporarily support the wall rock of the roadway, ensure the stability of the roadway wall rock, prevent roof collapse, and protect the safety of operators during roadway excavation. Many scholars have studied different forms of temporary support methods and their corresponding equipment

(1) Forepoling bar temporary support

A forepoling bar temporary support belongs to the passive support mode [8]. Generally, an I-beam for mining is used as the forepoling bar, which is suspended on the roof bolt in the support area and is probed to the newly cut, empty roof area along the direction of the roadway axis. The gap between the forepoling bar and the roof is filled with wooden wedges to ensure the contact between them.

The forepoling bar support has a certain protection effect on the roadway roof, the required equipment is simple, and the cost is low. However, the disadvantages of this support method are a poor support effect, complex erection process, long manual operation time, and low support efficiency [9]. Before the permanent support is completed, the rock mass has produced plastic deformation, which cannot effectively prevent roof accidents such as a roadway roof fall, and the support effect is not ideal [10]. During the erection of the forepoling bar support, the staff carry out the operation under the empty roof area, which makes it difficult to ensure the safety of the construction personnel [11].

(2) Machine-mounted temporary support

A machine-mounted temporary support is based on the roadheader and driven by the hydraulic cylinder, which is erected on the top of the roadheader to improve the adaptability of the temporary support to the roadway [12]. Li et al. [13] developed a new type of machine-mounted temporary support in view of the problems existing in the

temporary support with a forepoling bar. This equipment was designed with an integral shield beam and could operate alternately with the roadheader. Compared with the forepoling bar temporary support, this equipment was simple to operate and could exert an initial support force on the roadway roof, improve the roadway footage speed, and reduce the labor intensity of workers. Aiming at the problem of the long auxiliary time of bolt support in fully mechanized roadway excavation, Jian [14] developed a machine-mounted hydraulic temporary support composed of a guard plate, hydraulic cylinder, telescopic bar, and connecting rod. This equipment greatly improved the bolt support efficiency of the excavation head and the safety assurance system of the heading, improved the automation of the temporary support, and realized the rapid excavation of the roadway. Wang et al. [15] proposed a side slide temporary support. A telescopic guideway was installed on both sides of the roadheader, which was driven by a hydraulic cylinder. The temporary support moved to the empty roof area in front of the cutting section of the roadheader under the push of the telescopic guideway. A hydraulic cylinder was supported on the roadway floor, and the main guard plate contacted the roadway roof and provided the support force for it, which solved the problem that the support force of the temporary support on the roadway roof was limited by the advance's support distance. Li [16] developed a kind of temporary support matched with the EBZ160 roadheader, which could work under low roof conditions and solved the problem of the poor adaptability of the temporary support to a low roof roadway. Yan et al. [17] improved the side guard pin mounting base of a machine-mounted temporary support, reinforced it for the second time and designed a removable side guard mounting device, which solved the problem of the mounting base's variability and fracture. Xin [18] optimized the structure of the machine-mounted temporary support installed on the EBZ160 roadheader and installed a kind of frontal wall support device on the basis of the original machine-mounted temporary support, so that the temporary support could support both sides of the roadway and solved the problem that current machine-mounted temporary supports had difficulty supporting both sides of the coal wall.

Existing machine-mounted supports can play a certain supporting effect on the roadway roof, but there are some shortcomings, such as the inability to simultaneously carry out roof support and roadway excavation operations, and the inability to adapt to local uneven roof conditions.

(3) SmTS

Based on existing temporary support equipment and traditional hydraulic supports for roadways, Yang [19] designed an inchworm SmTS for coal mine roadways. This equipment realized the effective support of the roof and independent movement under the control of the hydraulic system, could move in parallel with the roadheader, and improved the adaptability of the SmTS to roadways with different sizes. Wang [20] proposed an SmTS composed of two groups of supports. This device moved by way of the two groups of supports supporting each other and moving forward alternately. It could realize the parallel operation of excavation and support, which improved the automation of temporary support. Yang [21] designed a walking equipment for a roadway, which realized the walking forward by sliding a guideway and two-way telescopic support. The equipment could realize automatic mesh laying and could cooperate with the bolt drill installed on the support to complete the permanent support of the roadway. Yao [22] designed a kind of SmTS which included a walking mobile support and hydraulic column and could provide temporary support and permanent support at the same time. The SmTS designed by Liu [23] was composed of eight single groups of supports, and the pushing device realized the step forward. The roof beam, side protection mechanism, and support leg were all independent structures, which improved the adaptability of the temporary support to the complex working conditions of the roadway.

(4) Mining–tunnelling–anchoring integrated machine

In recent years, Australia and America have made great progress in the research and development of mining anchor units that integrate mining, digging, and anchoring.

JOY company of Australia has designed the 12CM20WHRB-418 type digging and anchoring integrated unit, which is used for rapid roadway excavation and can carry out bolt support. The unit is equipped with four drilling rigs, which can realize the quick support of the roadway, but tunneling and support cannot be operated at the same time [24]. Another company has designed the ABM20 mining anchor unit. When cutting coal, the rear drill can provide temporary support for the roadway, which solves the problem that tunneling and anchor support cannot work at the same time [25]. In China, Shandong Yanzhou Coal Industry has developed an integrated machine for digging and anchoring, which realizes the integration of driving and permanent support, but both cannot work at the same time [26].

2.2. Finite Element Analysis of Temporary Support Equipment in Roadway

In order to solve structural mechanics problems, Professor Kraft first proposed the finite element analysis (FEA) method to study the structural strength of aircraft [27], which has become an effective method to solve complex engineering problems [28]. In order to meet the design requirements, a variety of analysis software based on FEA has been widely used to improve the efficiency of the analysis.

In recent years, many scholars have applied the FEA method to analyze the mechanical properties of various forms of temporary support equipment. Ren [29] carried out an FEA on the key load-bearing parts of the support, obtained the stress and strain distribution characteristics and vibration characteristics of the roof beam and base, checked the strength and stiffness of the key parts, and solved the resonance between the equipment and the roadheader. Lu [30] carried out a mechanical and modal analysis on the roof beam, base, and retaining wall of temporary support equipment of an arch roadway and obtained the strain and stress characteristics of key parts under the maximum wall rock pressure. Zhang [31] carried out an FEA on the overall structure and key bearing components of a temporary support under different working conditions according to industry standards. Li [32] carried out an FEA on the temporary support equipment under the roof fall condition of a rectangular roadway through ANSYS Workbench and verified that it met the support requirements. Yang [19] carried out an FEA on the roof beam and base of an inchworm-type tunnel temporary support and studied the stress and strain characteristics of the roof beam under normal working conditions and the most dangerous working conditions. Liu [23] verified the rationality of structural stiffness and strength through a static analysis, modal analysis, and dynamic response analysis of a single group of supports and a push mechanism.

2.3. Optimization of Temporary Support Equipment for Roadway

The optimal design was first derived from Maxwell's theory and Michell's truss optimization criteria. After that, VenLkayya and Gellatly proposed the optimal criteria method, and then F.G.E. Petersa proposed the full stress design method theory, which focused on how to improve the utilization of materials and reduce the weight of the structure while meeting the requirements of structural application. Fleury and Schmit [23] innovatively applied mathematical programming to optimization design problems and developed the ACCESS program system that could be used to solve optimization design problems. The system effectively improved the efficiency of solving structural optimization problems.

In recent years, more and more scholars have conducted relevant research on the optimal design of temporary supports. Ren [29] established the parametric model of the roof beam and base of the roadway SmTS and optimized its structure through ANSYS. By changing its parameters, stress concentration was avoided, and the structural stress was minimized on the basis of meeting the application requirements. Lu [30] took the roof beam of the temporary support as the optimization object, selected the distance between the two

bending plates in the roof beam as the design variable, and optimized the design with the goal of reducing the weight of the roof beam. After optimization, the roof beam weight was reduced by about 10%. Li [32] utilized the finite element method to optimize the roof beam steel bar mesh structure of the temporary support under the roof fall condition of a rectangular roadway, taking the number and diameter of the steel bar as the design variables, taking the minimization of quality as the optimization goal, and taking the initial number of the steel bar and the allowable stress of materials as the constraint conditions. After optimization, the overall quality of the roof beam was effectively reduced on the premise of meeting the support requirements. Du [10] optimized the structure of the roof beam of the temporary support. With the allowable stress and deformation of the materials as the constraint conditions, and the number and width of the I-beam and the section height of the roof beam as the design variables, the quality of the roof beam decreased by 11% after optimization. Ma [33] took the quality of the main beam of the SmTS as the optimization goal. Under the condition that the maximum equivalent stress of the structure was lower than the allowable stress of the material, he optimized the structure by adjusting the wall thickness of the main beam, reducing its the quality. Yan [34] took the roof beam of the temporary support of a rectangular roadway as the research object, analyzed the maximum deformation and maximum stress distribution characteristics of the roof beam under the roof fall condition, and avoided the structural stress concentration by improving the structural strength and optimizing the welding method. Li [35] optimized the structure by changing the number of I-beams of the temporary supports in the arch roadway, reducing the stress concentration of the roof beam structure, and solving the problem of equipment movement caused by stress concentration and excessive self-weight.

3. Mechanical Analysis and Numerical Simulation of Roadway Wall Rock

Before the tunnel is excavated, the rock at any place is squeezed by the wall rock. When the rocks are squeezed by each other, the rock at any place is in the original stress equilibrium state [36]. This state is broken when the roadway is opened. Due to the effect of wall rock pressure, the rock stress state is redistributed until a new equilibrium state is formed. The wall rock pressure is divided into the top pressure, side pressure, and bottom pressure [32], and they are affected by many factors, such as the nature of the wall rock, the shape of the roadway section, the size of the roadway section, and the buried depth of the roadway. As the roof rock falls, the temporary support supports the exposed roof to prevent the rock at the top of the roadway from continuing to fall, so that the rock at the top of the roadway acts on the temporary support by applying pressure. Excessive top pressure will cause roof fall accidents and threaten the safety of construction personnel.

Based on the analysis of the interaction between temporary support and wall rock, a solution method of a wall rock support system combining theoretical calculation and numerical simulation is proposed to determine the maximum wall rock pressure of the roadway, and the stress, displacement, and plastic failure characteristics of the roadway before and after the support is analyzed by numerical simulation, which provides a data basis for the subsequent support design, analysis, and optimization.

3.1. Wall Rock Support System and Its Mechanical Analysis

After the rock mass is damaged, during the redistribution of internal stress, the rock mass around the roadway plays a major bearing role on the overlying strata and is the main bearer of the wall rock pressure [37]. The temporary support only bears 1~2% of the weight of the overlying strata. Applying the initial support force to the exposed roof in time can effectively prevent the roof falling trend, prevent the continuous expansion of the wall rock plastic circle, and reduce the damage degree of the roof rock mass. The temporary support and wall rock constitute the wall rock support system, and their interaction relationship is shown in Figure 1. The abscissa U in the figure represents the displacement of wall rock, and the ordinate P represents the support force of the temporary support.

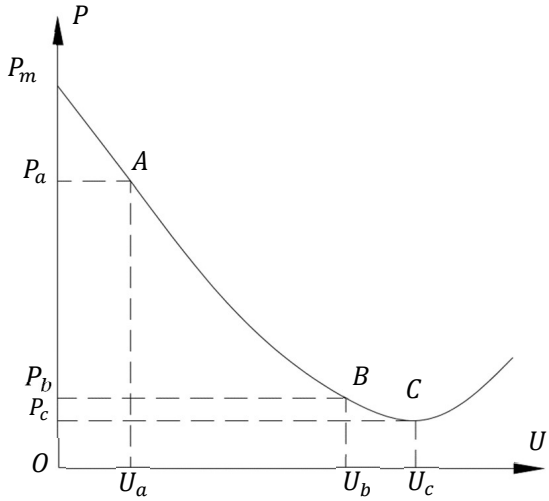

Figure 1. Interaction between temporary support and wall rock.

The original wall rock stress after roadway excavation is P_m, and only a temporary support providing a support force equivalent to P_m can completely prevent the roof from sinking. If a small amount of displacement of the roof is allowed, the roof is supported at point A. At this time, the displacement of the wall rock is U_a, and the support force required by the temporary support equipment is reduced to P_a, playing the role of self-bearing the wall rock. During the continuous sinking of the roof, the equipment working point is moved from point A to point B or point C, and the support force required by the equipment is also reduced to P_b and P_c. Therefore, in order to maximize the self-bearing effect of wall rock and reduce the support force required by the temporary support, it is required that the roadway support system have a certain strength and scalability, and the roof is allowed to have a certain displacement during the support process. The displacement U of the wall rock should be controlled within a reasonable range. When the displacement of the wall rock exceeds U_c, the loose pressure of the roadway increases, causing the wall rock of the roadway to become loose and collapse, and the support force of the temporary support equipment also increases. Therefore, in order to maximize the use of the self-bearing function of the wall rock and ensure the stability of the wall rock, the displacement of the wall rock should be controlled within U_c.

The design of a temporary support should be based on meeting the maximum wall rock pressure of the roadway, and the solution of the wall rock pressure is a necessary step in support design. At present, the theories related to wall rock pressure mainly include the whole soil column theory, circular section elastoplastic theory, Terzaghi's theory, PU's equilibrium arch theory, etc. Based on PU's equilibrium arch theory and Terzaghi theory, this paper adopted the method of comparing the two theoretical methods to solve the maximum wall rock pressure of the roadway and took a mining area as an example to carry out the mechanical calculation and analysis of the wall rock of the roadway.

(1) Solution of wall rock pressure based on PU's equilibrium arch theory

PU's equilibrium arch theory is a stress theory of wall rock that reflects the actual situation of roadway roof collapse proposed by Protochiakonov, and its calculation model is shown in Figure 2. According to this theory, the excavation of a roadway in a loose rock mass with a certain cohesion forms a natural equilibrium arch at its top. The wall rock pressure exerted on the temporary support is the self-weight of the rock mass inside the natural equilibrium arch. The rock mass inside the equilibrium arch cannot bear the tensile stress but can only bear the compressive stress [38]. A sliding surface with a certain angle to the vertical plane is formed on both sides of the roadway.

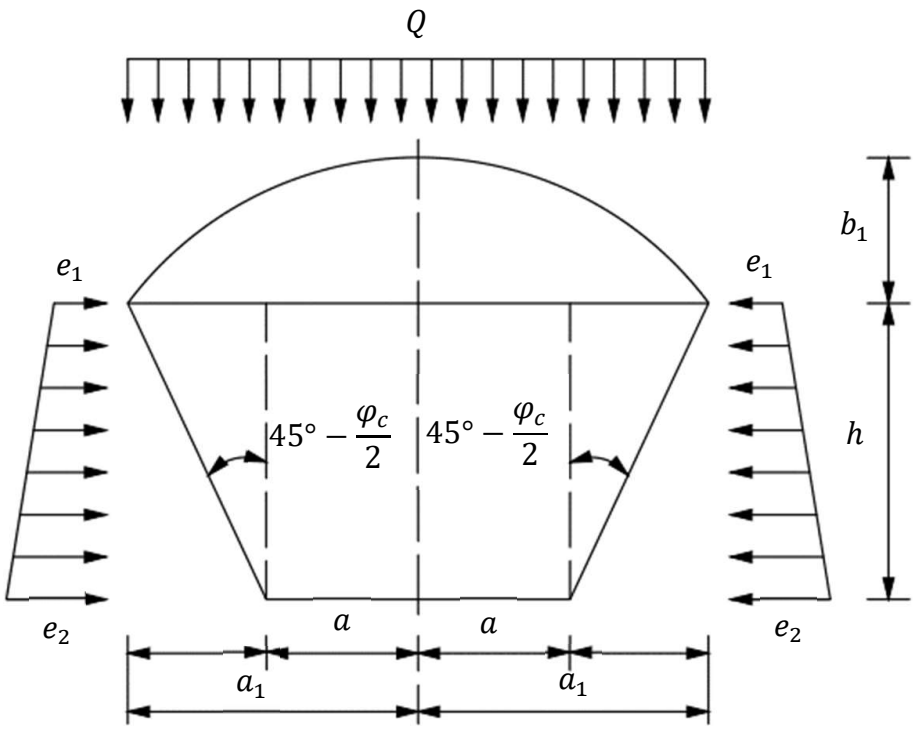

Figure 2. Theoretical calculation model of equilibrium arch.

According to the theoretical calculation model, when the side wall of the roadway is unstable, the maximum rise b_1 of the natural balance arch is as follows

$$b_1 = \frac{a_1}{f_p} \tag{1}$$

where a_1 is the half-span of the natural balanced arch and f_p is the rock mass firmness coefficient.

The maximum span of natural balanced arch $2a_1$ is:

$$2a_1 = 2\left[a + h\tan\left(45° - \frac{\varphi_c}{2}\right)\right] \tag{2}$$

where a is the half-width of the roadway; h is the roadway height; and φ_c is the angle of internal friction of the rock mass.

The maximum wall rock pressure Q is:

$$Q = \gamma b_1 \tag{3}$$

where γ is the average weight of the rock mass.

(2) Solution of wall rock pressure based on Terzaghi's theory

Based on the principle of stress transmission, Terzaghi's theory [39] believes that the wall rock pressure acting on temporary support equipment comes from the stress transmission of the self-weight of the overlying soil, and the size of the wall rock pressure depends on such factors as the self-weight of the soil in the loose area and the internal friction angle of the rock mass [40]. In this theory, the differential element body is taken in the sliding block for the stress analysis, and the maximum wall rock pressure of the roadway is calculated. The calculation model is shown in Figure 3.

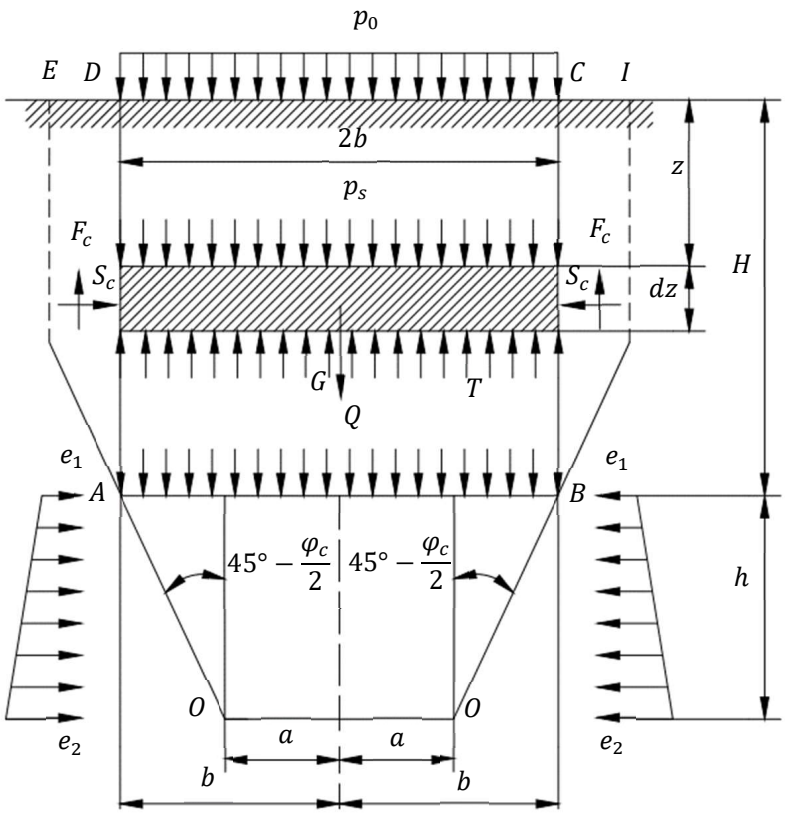

Figure 3. Terzaghi's theoretical model.

In the Terzaghi's calculation model, when the overlying strata subside, the two sides of the roadway form a staggered surface. The included angle between OA and OB and the vertical plane in Figure 3 is $45^{\circ} - \varphi_c/2$. The staggered surface starts at point O of the roadway floor, reaches points A and B along curve OA and OB, and then reaches points E and I along curve AE and BI. The trajectory of curve AE and BI is difficult to calculate. Generally, approximate vertical curves AD and BC are used to replace curves AE and BI, respectively. The area $ABCD$ between the roadway top and the ground is the sliding block, and its width $2b$ is as follows

$$2b = 2\left[a + h\tan\left(45^{\circ} - \frac{\varphi_c}{2}\right)\right] \tag{4}$$

where b is the half-width of the sliding block.

The differential element body with a thickness of dz and a buried depth of z is cut in the sliding block. The stress of the element body is shown in Figure 3. The overburden rock pressure P_s applied vertically downward on the upper surface of the unit is as follows

$$P_s = 2bq_r \tag{5}$$

where q_r is the vertical initial geostress.

The dead weight G of the unit is:

$$G = \int 2b\gamma dz \tag{6}$$

where dz is the unit thickness.

The vertical uplift force T applied on the lower surface of the unit is as follows

$$T = \int 2b(q_r + dq_r) \tag{7}$$

The vertical sidewall rock friction F_c applied on the side of the unit is as follows

$$F_c = \int (k_0 q_r \tan \varphi_c + c) dz \tag{8}$$

where c is the cohesion of the rock mass and k_0 is the coefficient of side pressure.

The balance condition of the unit in the vertical direction is as follows

$$\sum F_r = P_s + G - T - 2F_c \tag{9}$$

By introducing Formulas (7)–(10) into Formula (11), we get the following

$$q_r = \frac{b\gamma - c}{k_0 \tan \varphi_c} \left(1 + Ae^{-\frac{k_0 z \tan \varphi_c}{b}}\right) \tag{10}$$

where z is the buried depth of the unit.

According to the characteristics of Terzaghi's theoretical model, when $z = 0$, $q_r = P_0$, and P_0 is the additional load on the surface. P_0 is calculated as follows

$$P_0 = \frac{b\gamma - c}{k_0 \tan \varphi_c}(1 + A) \tag{11}$$

Substituting Formula (13) into (12), we get the following

$$q_r = \frac{b\gamma - c}{k_0 \tan \varphi_c} \left(1 - e^{-\frac{k_0 z \tan \varphi_c}{b}}\right) + P_0 e^{-\frac{k_0 z \tan \varphi_c}{b}} \tag{12}$$

Taking $z = L$ into Formula (14), the maximum wall rock pressure Q can be obtained as follows

$$Q = \frac{b\gamma - c}{k_0 \tan \varphi_c} \left(1 - e^{-\frac{k_0 L \tan \varphi_c}{b}}\right) + P_0 e^{-\frac{k_0 L \tan \varphi_c}{b}} \tag{13}$$

where L is the roadway burial depth.

(3) Calculation of wall rock pressure in the 7900 mining area belt roadway

The section of the belt roadway in the 7900 mining area of a mine is rectangular, and its relevant parameters are shown in Table 1. The maximum wall rock pressure of the roadway is calculated based on the above-mentioned PU's equilibrium arch theory and Terzaghi's theory.

Table 1. Parameters of 7900 mining area belt roadway.

Roadway Parameters	Values
Height: h	3.5 m
Span: $2a$	4.5 m
Cross-sectional area: S	15.75 m^2
Burial depth: L	60 m
Average weight density of rock mass: γ	25 KN/m^3
Rock firmness coefficient: f_p	3
Lateral pressure coefficient: k_0	1
Internal friction angle of rock mass: φ_c	30°

Based on PU's equilibrium arch theory, the maximum span $2a_1$ of the natural equilibrium arch was 8.54 m according to Formula (2), the maximum rise height b_1 of the natural equilibrium arch was 1.423 m according to Formula (1), and the maximum wall rock pressure Q of the roadway was 0.0355 MPa according to Formula (3). Based on Terzaghi's theory, the width $2b$ of the sliding block was calculated as 8.54 m by Equation (4), and the cohesive force of the loose soil is usually 0.2 MPa. Regardless of the surface additional load

P_0, the maximum wall rock pressure Q of the roadway was calculated as 0.032 MPa by Equation (13).

In order to ensure the safety and effectiveness of the temporary support and ensure that the temporary support can provide a sufficient support force for the wall rock of the roadway, the larger value of 0.0355 MPa calculated by PU's equilibrium arch theory and Terzaghi's theory was taken as the maximum wall rock pressure of the roadway as the basis for subsequent calculations.

3.2. Numerical Simulation of Roadway Wall Rock Based on FLAC 3D

In view of the complex geological conditions of the coal mine roadway, it was difficult for the theoretical calculation to accurately reflect the real stress, deformation, and displacement of the wall rock support system in the roadway. A numerical simulation method of roadway wall rock support system based on FLAC 3D was constructed to analyze the stress, displacement, and plastic failure characteristics of the roadway roof before and after temporary support.

A numerical simulation method can fully reflect the stress, displacement, plastic failure, and other characteristics of the wall rock within the range of the geotechnical model and can modify the model parameters according to the actual situation of the rock mass to simulate the different working conditions and geological conditions of the wall rock. Common numerical simulation methods include the finite element method, boundary element method, finite difference method, etc. Among them, the finite difference method uses a difference instead of the differential, uses a Taylor series method to replace the differential quotient in the original equation and the conditions of a definite solution, and uses an integral sum to replace the integral, so as to establish difference equations instead of differential equations, which is more suitable for geotechnical research [41].

Rock has the properties of a high compressive strength but low tensile and shear strength, and the stress–strain relationship of the rock mass has complex nonlinear characteristics. The rock mass bearing complex stress will have different forms of damage, plastic failure, weak plane shear failure, etc. Based on the generalized concept of plasticity theory, the above failure forms of the rock mass can be considered as "plastic failure", so the corresponding constitutive relationship can be established by using the plasticity theory. Before reaching the yield limit, the medium can be approximately regarded as elastic, and after reaching the yield limit, it can be regarded as plastic. When the material reaches the strength limit, it is destroyed, and plastic flow occurs. The Mohr–Coulomb plastic failure criterion model can better represent the stress failure characteristics of a soil mass and is generally used for underground excavation and slope stability analysis. Its theory is that materials change from elastic deformation to plastic deformation [42], and yield failure occurs when the stress reaches the yield limit. Its yield function is as follows

$$\left|\tau_q\right| = c + \sigma_n \tan\varphi \tag{14}$$

where τ_q is the shear force of the yield surface and σ_n is the yield surface normal stress.

The parameters of the Mohr–Coulomb plastic failure criterion model mainly include bulk modulus (K), shear modulus (G), Young's modulus €, and Poisson's ratio (μ). The relationship between these parameters is as follows

$$K = \frac{E}{3(1-2\mu)} \tag{15}$$

$$G = \frac{E}{2(1+\mu)} \tag{16}$$

In the numerical simulation of roadway wall rock, the commonly used geotechnical analysis software includes FLAC 3D, UDEC, 3DEC, etc. FLAC 3D was selected as the software foundation to build our numerical simulation method of a roadway wall rock support system. It is based on the Lagrangian finite difference method, which can accurately

simulate the yield and plastic flow of materials and can effectively deal with elastoplastic materials, large deformation, and other problems, which is suitable for the research content of this paper.

The size of the elastic–plastic area and stress concentration area during roadway excavation is affected by factors such as the roadway section size, burial depth, and mechanical properties of coal and rock. Combined with the geological data of the 7900 mining area of a mine, FLAC 3D was used to build the roadway wall rock support system model, as shown in Figure 4, wherein (a) is the initial model of wall rock and (b) is the model of roadway after excavation. The length of the model was 20 m, the width was 9 m, and the height was 16 m. The shape of the roadway section was rectangular, and the section size was 4.5 × 3.5 m, with a section area of 15.75 m^2; it was composed of four layers of siltstone, coal seam, silty sandstone, and medium fine sandstone from bottom to top. The definition of its geological data is shown in Table 2.

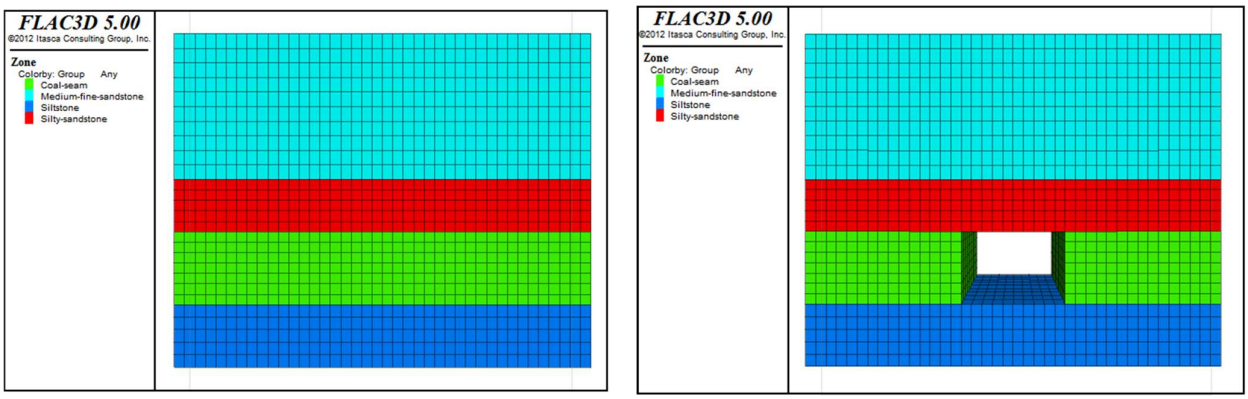

(**a**) (**b**)

Figure 4. Roadway wall rock- support system model. (**a**) Initial model of wall rock, (**b**) excavation roadway model.

Table 2. Rock mass parameters of wall rock model.

Rock Type	Thickness (m)	Cohesion (MPa)	Internal Friction Angle (°)	Density (kg/m^3)
Siltstone	3.0	7.2	35.0	2730
Coal seam	3.5	1.1	32.3	1330
Silty sandstone	2.5	5.6	38.4	2815
Medium fine standstone	7	7.0	40.5	2615

The wall rock model grid was divided unevenly, and the wall rock model grid parameters are shown in Table 3.

Table 3. Grid parameters of wall rock model.

Rock Type	Length (m)	Width (m)	Height (m)
Siltstone	0.5	0.2	0.6
Coal seam	0.5	0.2	0.5
Silty sandstone	0.5	1.0	0.5
Medium fine standstone	0.5	1.0	0.7

We defined the boundary conditions of the roadway model as shown in Formula (17):

$$\begin{cases} \Delta_{x1} = 0 \\ \Delta_{x2} = 0 \\ \Delta_y = 0 \\ q_f = 1.5 \text{ MPa} \end{cases} \tag{17}$$

where Δ_{x1} is the lateral horizontal displacement of the model side, Δ_{x2} is the horizontal displacement of the model bottom, and Δ_y is the vertical displacement of the model bottom. q_f is the overburden load on the model top, as defined in Formula (18).

$$q_f = \sum_{i=1}^{n} \gamma_i L_i \tag{18}$$

where γ_i represents the unit weight of each rock layer, L_i represents the thickness of each rock layer, i represents different rock layers above the roadway, and n represents the total number of rock layers. Here, the value of γ_i is 25 KN/m^3, which is the average value.

We ran FLAC 3D to conduct a numerical simulation on the roadway wall rock model established above, and we analyzed the displacement, stress, and plastic failure characteristics of the roadway roof before and after the temporary support equipment support according to the operation results. The support force required for the roadway roof was calculated in Section 3.1. Here, we added this support force to the lower surface of the roadway roof to replace the actual support. In this process, the influence of support stiffness on the roof was ignored.

(1) Distribution characteristics of vertical displacement of roadway roof

The vertical displacement distribution of the roadway roof before and after temporary support is shown in Figure 5. The comparative analysis of (a) and (b) shows that the maximum vertical displacement of the roof before the support was 2.14 mm, the maximum vertical displacement of the roof after the support was 1.76 mm, and the maximum vertical displacement of the roof after the support was 17.8% lower than before, indicating that the temporary support could protect the roof and reduce the roof subsidence.

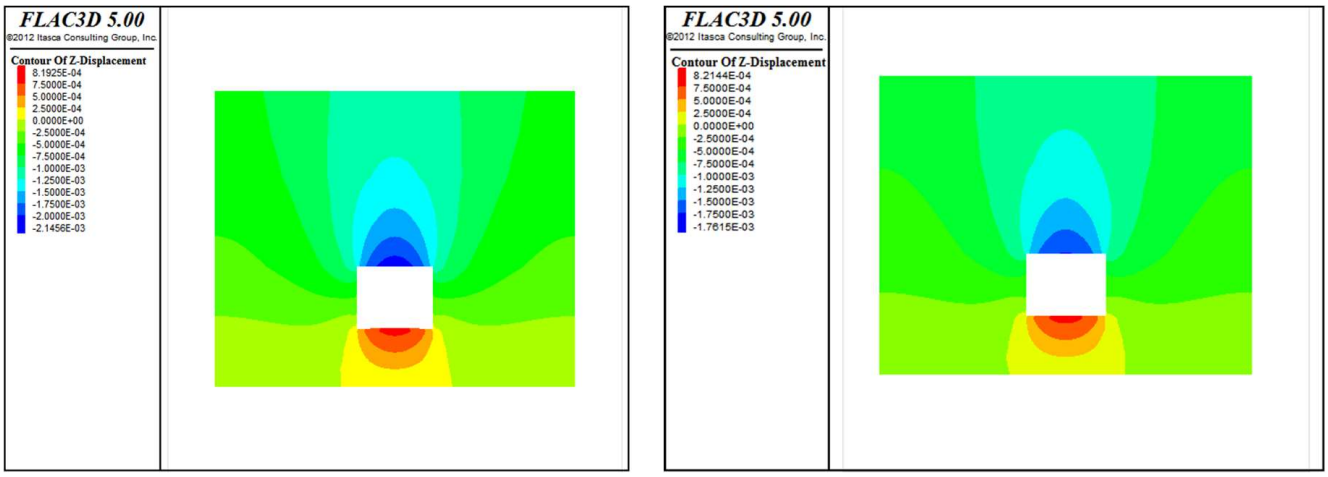

(**a**) (**b**)

Figure 5. Vertical displacement distribution of roadway roof. (**a**) Before support, (**b**) after support.

The vertical displacement curve of the roadway roof before and after temporary support is shown in Figure 6. The comparative analysis of (a) and (b) shows that the vertical displacement of the wall rock on both sides of the roadway was small, indicating that the wall rock on both sides of the roadway had a strong bearing capacity. The closer to the roadway center, the greater the roof displacement. At x = 7.75 m and x = 12.25 m, that is, at the side wall of the roadway, the vertical displacement of the roof increased rapidly. After the roof had been supported, the overall displacement trend of the roof was not obvious, the overall displacement of the roof was controlled, and the displacement control effect in the middle area of the roof was most obvious.

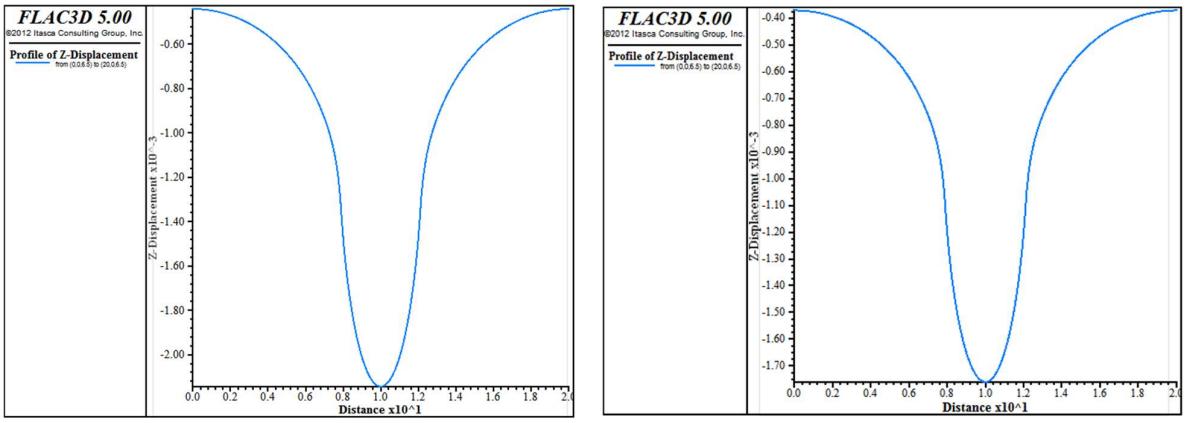

(**a**) (**b**)

Figure 6. Vertical displacement curve of roadway roof. (**a**) Before support, (**b**) after support.

(2) Stress distribution characteristics of roadway roof

The stress distribution characteristics of the roadway roof before and after temporary support are shown in Figure 7. The wall rock in the middle of the roof mainly bore tensile stress, while the wall rock in other areas mainly bore compressive stress. According to the rock properties, the wall rock in the middle of the roof was most likely to be deformed and damaged. By comparing (a) and (b), it can be seen that the maximum horizontal stress of the roof before the support was 0.56 MPa, and the maximum horizontal stress of the roof after the support was 0.35 MPa. The maximum stress of the roof was 36.5% lower than before, indicating that the stress of the roof was controlled under the support of the temporary support equipment.

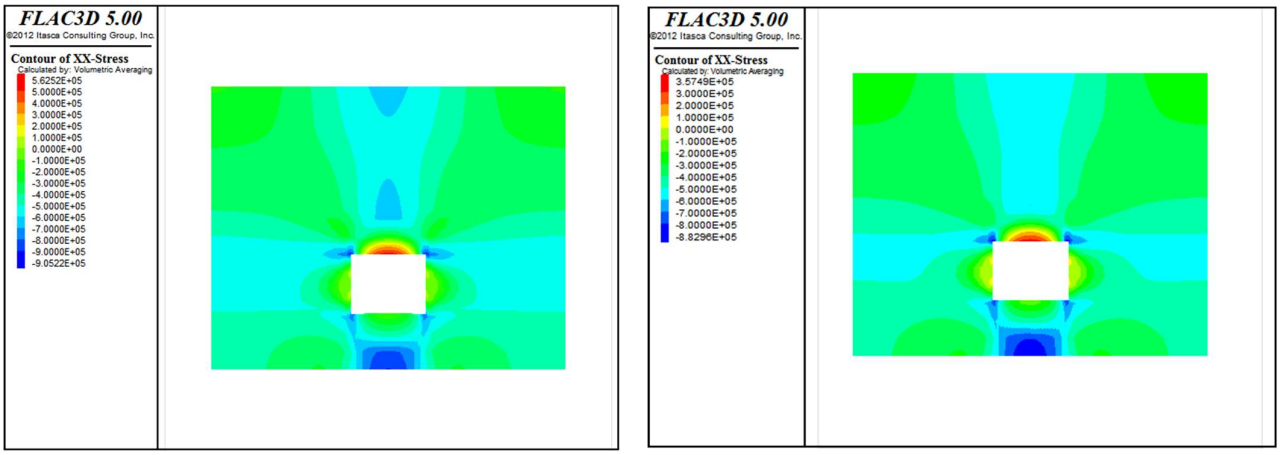

(**a**) (**b**)

Figure 7. Roadway roof stress distribution. (**a**) Before support, (**b**) after support.

The stress curve of the roadway roof before and after temporary support is shown in Figure 8. The wall rocks on both sides of the roadway mainly bore compressive stress, and the wall rocks in the empty roof area mainly bore tensile stress. The closer the roof was to the roadway, the greater the compressive stress was. At x = 7.75 m and x = 12.25 m, that is, at the side wall of the roadway, the stress trend of the roof changed, the compressive stress decreased, and the compressive stress changed to a tensile stress. After the support, the roof stress was reduced, and the stress control effect of wall rock in the empty roof area was the best. According to the physical characteristics of rock with a strong compressive capacity but poor tensile capacity, the tensile stress of the roof was reduced after support,

which indicated that temporary support equipment played a certain role in protecting the roof wall rock.

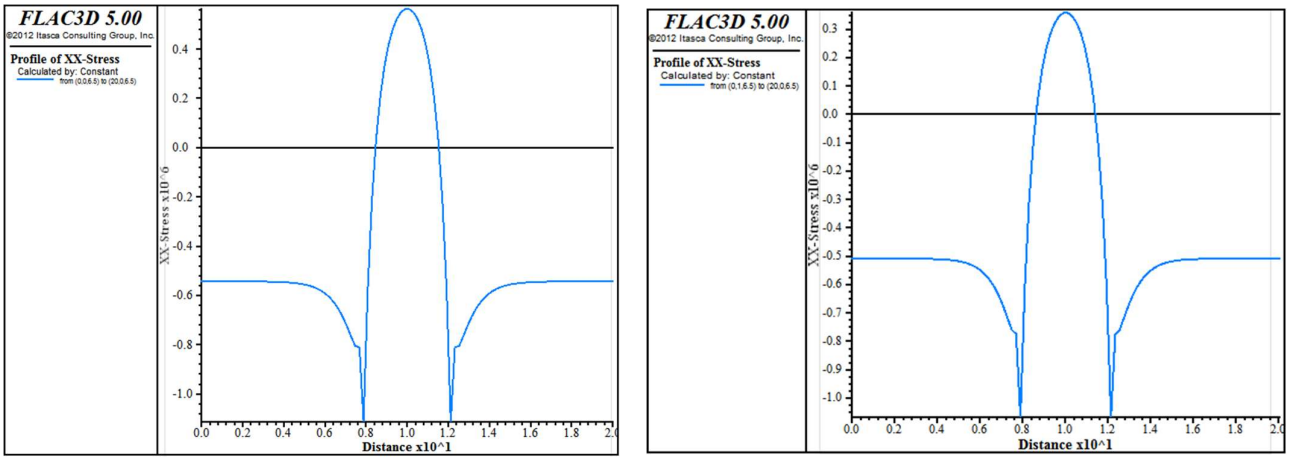

(**a**) (**b**)

Figure 8. Stress curve of roadway roof. (**a**) Before support, (**b**) after support.

(3) Plastic failure characteristics of roadway roof

The plastic failure characteristics before and after roadway roof support are shown in Figure 9.

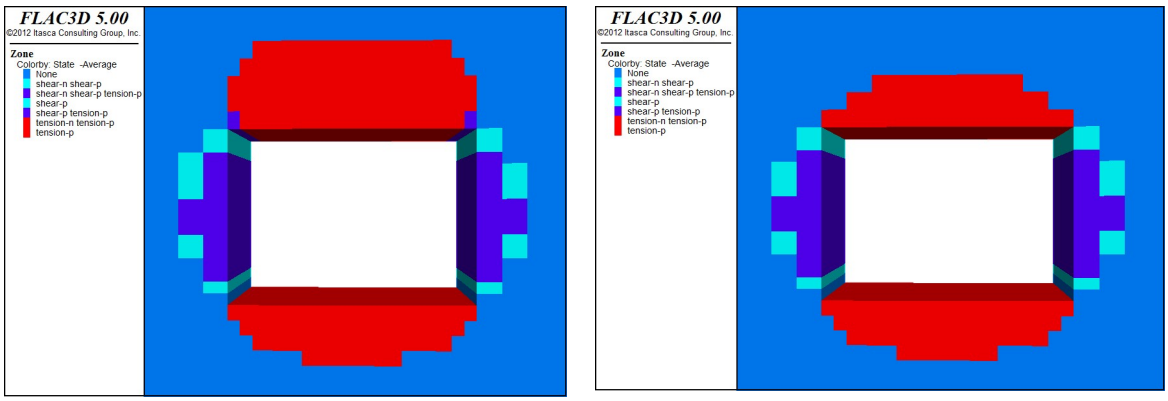

(**a**) (**b**)

Figure 9. Distribution of plastic failure of roadway roof. (**a**) Before support, (**b**) after support.

After the roadway is excavated, the internal stress of the wall rock is released, and the stress release process will cause the plastic failure of the roadway roof, floor, and two sides to varying degrees. The comparative analysis of (a) and (b) shows that the application of temporary support reduced the plastic failure area of the roof, indicating that the plastic failure trend of the roof was controlled to a certain extent, preventing the continuous expansion of the plastic circle of the wall rock; it showed that the temporary support could prevent further damage of the roof wall rock.

4. SmTS Scheme and Its Mechanical Characteristics Analysis

Based on the preceding mechanical analysis of the wall rock support system of the roadway, in order to adapt to the actual working conditions of the coal mine roadway, an SmTS scheme for the tunneling roadway is proposed, and the SmTS is designed. On the basis of adapting to the actual working conditions of the coal mine roadway, the effective

protection of the roadway is realized. The mechanical properties of the support are studied based on the finite element method to ensure the bearing capacity of the support.

4.1. Structural Design and Implementation of SmTS

The SmTSs mentioned in [20,30,33] do not consider the uneven working condition of the roadway roof. Under this working condition, the temporary support cannot fully contact the roadway roof, so it is easy to have uneven stress in the support process. In order to achieve effective roof support, a kind of SmTS that can adapt to uneven roof conditions was designed based on the previous research, as shown in Figure 10. The equipment mainly includes a main beam, column, base, side guard board, four-bar mechanism, push jack, side guard board jack, and other mechanisms. This equipment adopts the form of two groups of support frames, which support each other and move forward alternately. Considering that the SmTS is subjected to a horizontal force during moving, a four-link mechanism has been installed between the equipment main beam and the base to prevent the equipment from tipping.

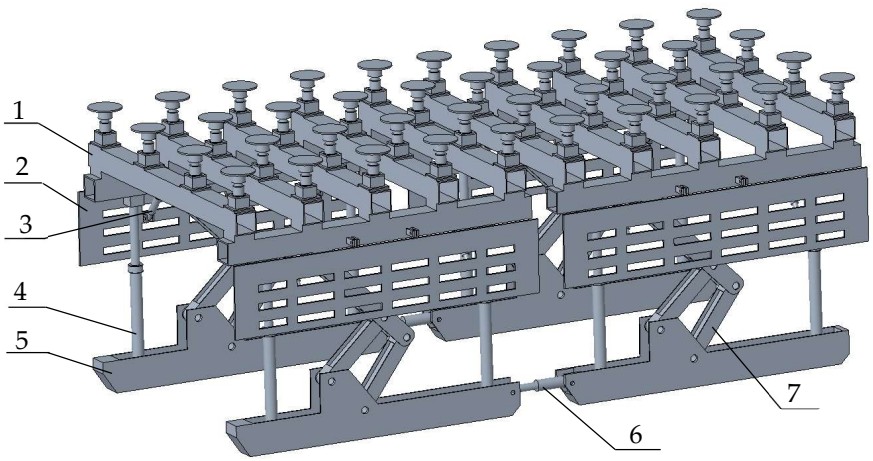

Figure 10. Structural diagram of SmTS. 1. Main beam; 2. side guard plate; 3. side guard plate jack; 4. column; 5. base; 6. moving jack; 7. four-bar linkage.

The roadway section supported by the SmTS is rectangular. In order to prevent the roadway roof from falling, the top of the equipment bears the top pressure generated by the weight of the overlying rock, that is, the maximum wall rock pressure. The top pressure is the main factor of roadway damage. Taking the roof as the key support object of the SmTS, when the top pressure is transferred to both sides of the roadway, it causes the rocks on both sides to squeeze into the roadway. Both sides of the equipment bear the lateral wall rock pressure generated when the two sides of rocks are squeezed.

The SmTS drives the roof beam and side shield through the column and side shield jack to provide a support force for the roadway roof and side wall formed by the new cutting, so as to prevent the roadway from large deformation, collapse, and other damage, reduce the disturbance to the roadway roof, and prepare for the subsequent permanent support.

This kind of SmTS consists of two support groups at the front and back, which are connected by pushing jacks. The front and rear support groups support each other and move forward alternately. The pushing process is as follows:

(1) The piston rod of the side guard jack on both sides of the front support group shrinks, the side guard is separated from the coal wall, the column of the front support group drops, and the main beam is separated from the roof.
(2) The rear support group is the support, the jack piston rod is pushed out, and the front support group pushes forward for one step. After the forward movement, the support is shown in Figure 11.
(3) The column of the front support group rises, the main beam rises and supports the top plate, the side guard jack pistons on both sides of the front support group stretch

out, the side guard supports the coal wall, and the front support group completes the push frame.

(4) The piston rod of the side guard jack on both sides of the rear support group shrinks, the side guard is separated from the coal wall, the rear support group column drops, and the main beam is separated from the roof.

(5) The front support group is the support. The jack piston rod is pushed to retract, and the rear support group is pulled to move forward for one step. After the forward movement, the support is shown in Figure 12.

(6) The column of the rear support group rises, the main beam rises and supports the top plate, the jack piston of the side guard plate of the rear support group stretches out, and the side guard plate supports the coal wall. A push cycle is completed.

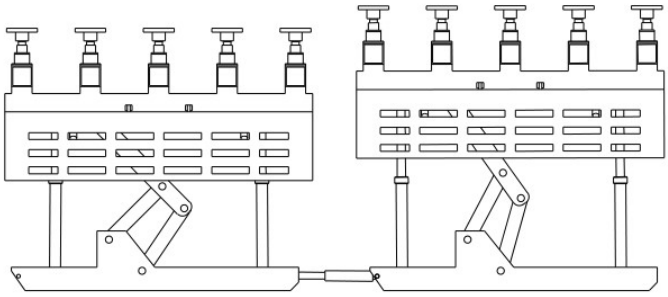

Figure 11. State diagram of front support group.

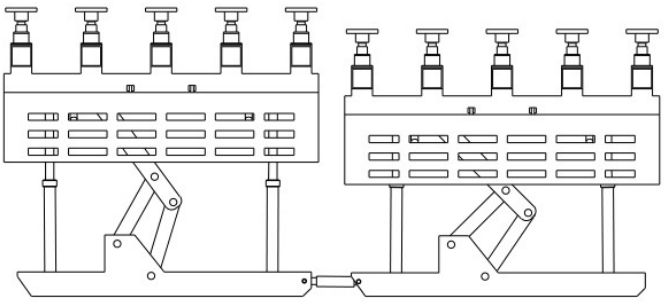

Figure 12. State diagram of rear support group.

The SmTS can move forward in parallel with the roadheader. After the roadheader excavates the empty roof area, the SmTS can support the empty roof area in time to prevent the roof from falling, improve the roadheader startup rate, and improve the support efficiency.

4.2. Adaptability Analysis of SmTS

The environment of a coal mine roadway is complex, and the temporary support not only needs to meet the needs of wall rock support, but also should work in parallel with other equipment in the roadway.

4.2.1. Adaptability Analysis of Support and Other Equipment in Roadway

The SmTS "straddles" the roadheader, which does not affect the normal operation of the roadheader and other equipment. Sufficient space is reserved for the subsequent permanent support and ventilation. On the premise of not interfering with the normal cutting of coal and rock mass by the roadheader, the roadway roof and both sides are temporarily supported, and can cooperate with the roadheader, conveyor, and other equipment to form the roadway heading working face system, as shown in Figure 13.

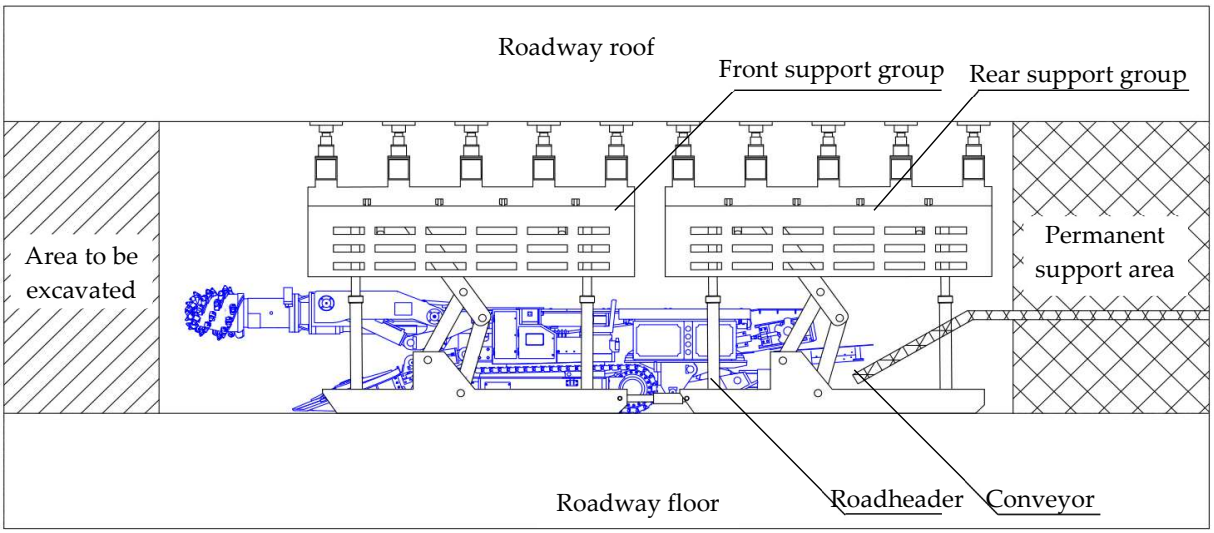

Figure 13. Roadway heading face system.

4.2.2. Analysis on Adaptability of Support to Roadway Roof

As one of the main load-bearing components of the temporary support, the roof beam bears the roof load, which has the function of supporting and protecting the roof, so it has a high strength and stiffness. In order to adapt to the local uneven working condition of the roadway roof, the roof beam adopts a flexible design, which is composed of a main beam and adaptive support mechanism, shown in Figure 14.

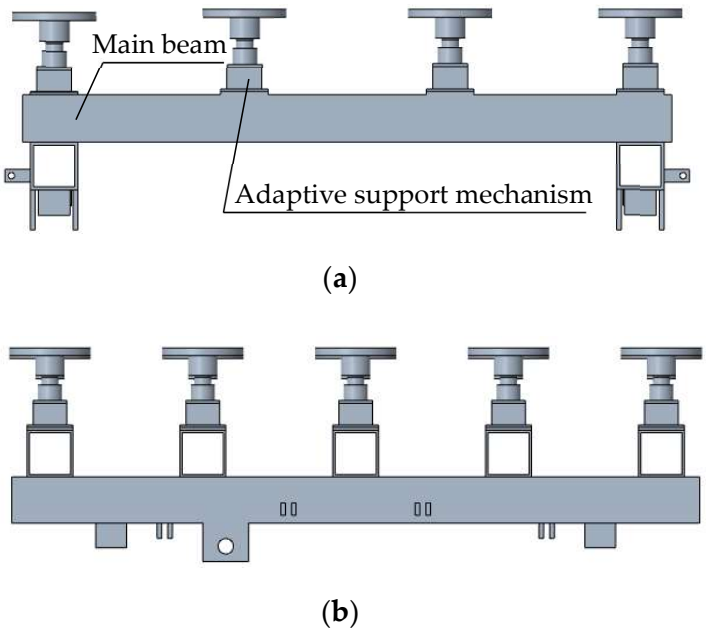

Figure 14. Roof beam structure. (**a**) Front view, (**b**) side View.

The adaptive support mechanism is composed of a support plate, flange plate, lifting sleeve, compression spring, limit plate, and fixed sleeve, as shown in Figure 15. The support plate is in contact with the roadway roof, its lower end is hinged with the lifting sleeve, the compression spring is fixed inside the lifting sleeve and the fixed sleeve, and the adaptive support mechanism is fixed on the spring support of the main beam.

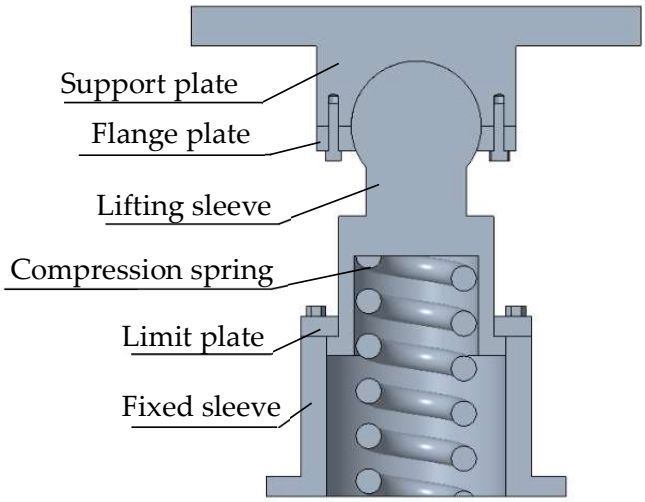

Figure 15. Adaptive support mechanism.

Under the working condition of an uneven roof, the working principle of adaptive support mechanism is shown in Figure 16.

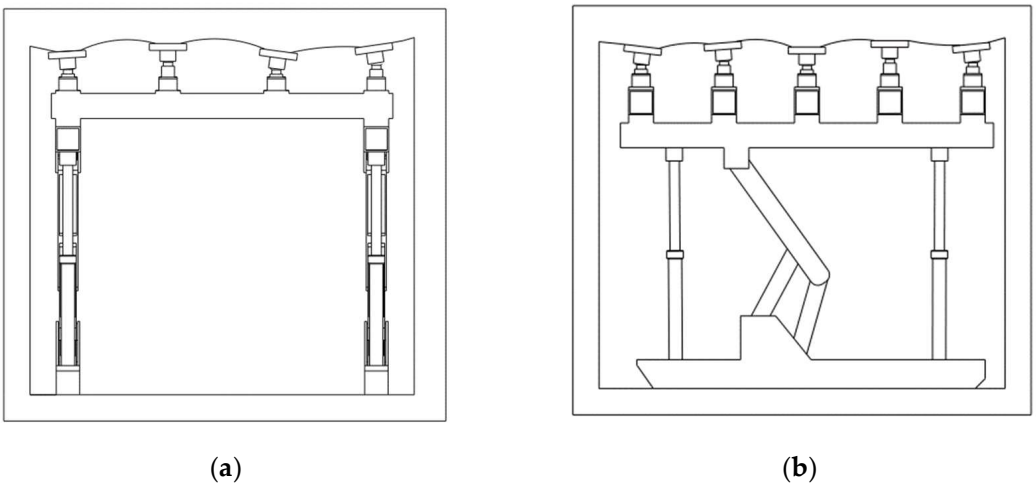

Figure 16. Working principle of adaptive support mechanism. (**a**) Front view, (**b**) side view.

When the roof beam contacts the roadway roof, the uneven roof condition makes the main beam unable to fully contact the roof. Through the adaptive support mechanism installed on the main beam, its support plate can adapt to the local inclination of the roof, and through the lifting sleeve and compression spring, it can adapt to the local unevenness of the roof, ensure the contact between the roof beam and the roof, and apply the initial support force.

4.3. Design Example of SmTS

We took the belt roadway in 7900 mining area of a mine mentioned above as an example to design the temporary support. The EBZ135 roadheader was used for the roadway excavation, and its relevant parameters are shown in Table 4. According to the roadway size shown in Table 1 and the maximum wall rock pressure of 0.0355 MPa calculated previously, we determined the overall size parameters, support strength, and working resistance of the SmTS.

Table 4. Parameters of EBZ135 roadheader.

Parameter	Value
Total length	8.92 m
Overall width	2.83 m
Total height	1.48
Cutting height	4.0 m
Cutting width	5.1 m
Cutting area	20.5 m^2
Cutting head speed	44 rpm
Travel speed	0~6.6 m/min

(1) SmTS parameters

In order to obtain the best support effect, the main beam of the support must fit the roadway roof. The maximum support height of the support equipment was 3.5 m. To ensure that the roof beam did not interfere with the cutting operation of the roadheader, the lowest position of the roof beam was 1.5 m higher than the height of the roadheader, so the minimum support height of the temporary support was 3 m.

The side guard board fitted the two sides of the roadway to obtain the best support effect, that is, the overall width of the equipment was equal to a roadway width of 4.5 m. In order not to affect the normal layout of the roadheader and realize the parallel operation of the temporary support and the roadheader, the horizontal distance between the two bases of the temporary support should be greater than the total width of the roadheader, and the horizontal distance between the two bases was taken as 3.4 m.

The temporary support straddled the roadheader to fully cover the roadheader. The length of the temporary support had to be greater than the total length of the roadheader. Considering that the roadheader needs to leave working space for permanent support when it retreats, the total length of the temporary support was determined to be 9 m. The equipment consisted of two support groups, and the length of a single support group was 4.5 m.

(2) Support strength and working resistance of SmTS

The support strength was calculated as follows

$$q_0 = \frac{QS_k}{S_l} \tag{19}$$

where q_0 is the support strength, S_l is the contact area between the main beam and top plate, S_k is the top control area, and its definition is shown as follows

$$S_k = 2L_d a \tag{20}$$

where L_d is the length of single support group.

According to Formula (24), the top control area of SmTS was 20.25 m^2, the maximum wall rock pressure Q was calculated as 0.0355 MPa previously, and S_l was 6.18 m^2. The support strength q_0 was obtained according to Formula (23), which was 0.116 MPa.

The working resistance of SmTS F_0 was:

$$F_0 = Q \times S_k \tag{21}$$

When the parameter was brought into Formula (25), F_0 was 720 KN.

4.4. Mechanical Characteristics Analysis of SmTS

On the basis of theoretical calculation, a computer simulation was carried out for the support equipment designed in Section 4.3 to verify the reliability of the design.

4.4.1. Static Analysis of SmTS

ANSYS Workbench was used as an analysis tool to simulate the stress and deformation of key components such as the main beam of the support under different working conditions. Taking the main beam as an example, the main beam was made of two longitudinal and five transverse rectangular steel tubes. The width and height of the steel tubes were 300 mm, and its thickness was 25 mm. The length of the longitudinal and transverse steel tube was 4.5 m and 4.1 m, respectively. The transverse steel tubes were uniformly distributed on the longitudinal steel tubes. We set the material to Q550, and its parameters were set as follows: the elastic modulus was 210 GPa, Poisson's ratio was 0.3, the yield strength was 550 MPa, and the tensile strength was 670 MPa. We set the cell type as a tetrahedron mesh, and the mesh cell size was 50 mm.

We set the boundary conditions of the main beam as follows. According to the working resistance of 720 kN of the support obtained in Section 4.3, we evenly distributed it to four columns, and the support force of each column was 180 kN. The working resistance of the support was calculated under six typical working conditions of the main beam, including uniform loading, loading at both ends, loading at both sides, lateral eccentric loading, longitudinal eccentric loading, and torsional loading. Its load is shown in Figure 17.

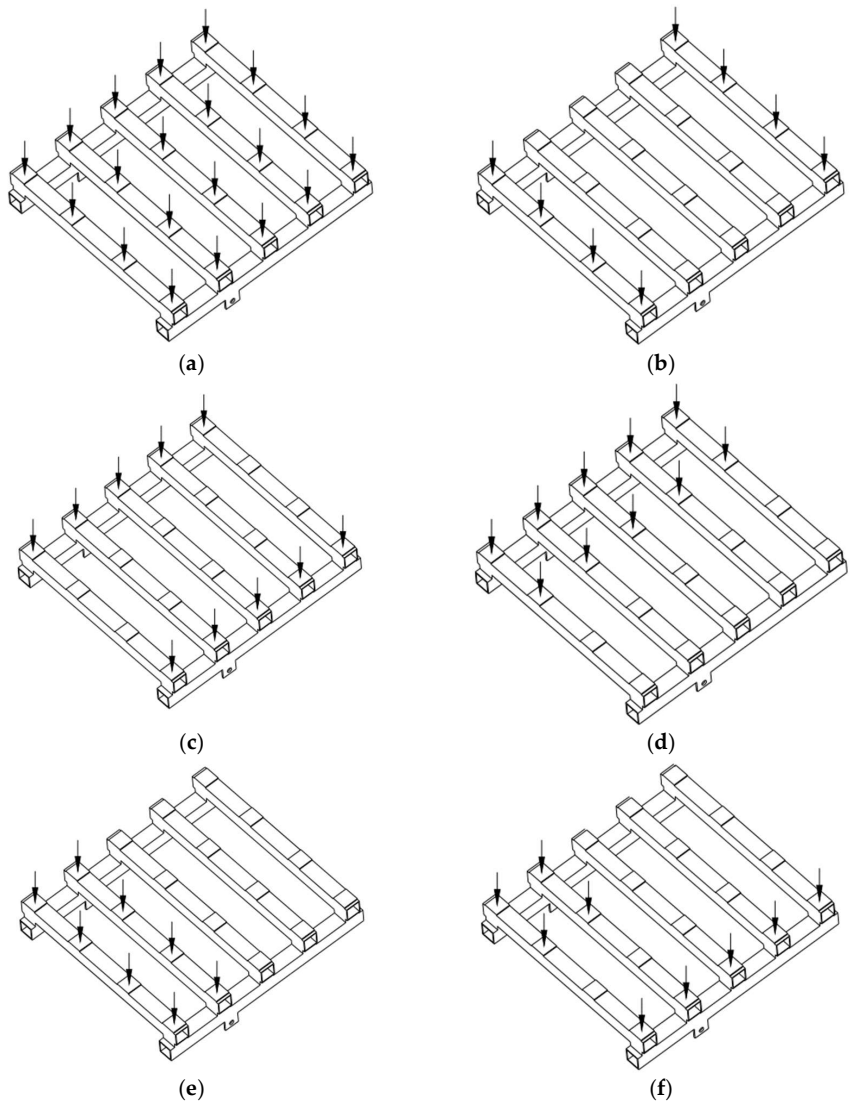

Figure 17. Six typical working conditions of the main beam. (**a**) Uniform loading, (**b**) loading at both ends, (**c**) loading on both sides, (**d**) lateral eccentric loading, (**e**) longitudinal eccentric loading, and (**f**) torsional loading.

In the Static Structural module of ANSYS Workbench, the stress conditions of the main beam under the above six working conditions were solved. The stress and deformation nephogram of the main beam is shown in Figure 18, and the maximum stress and deformation are shown in Table 5. The conclusions are as follows.

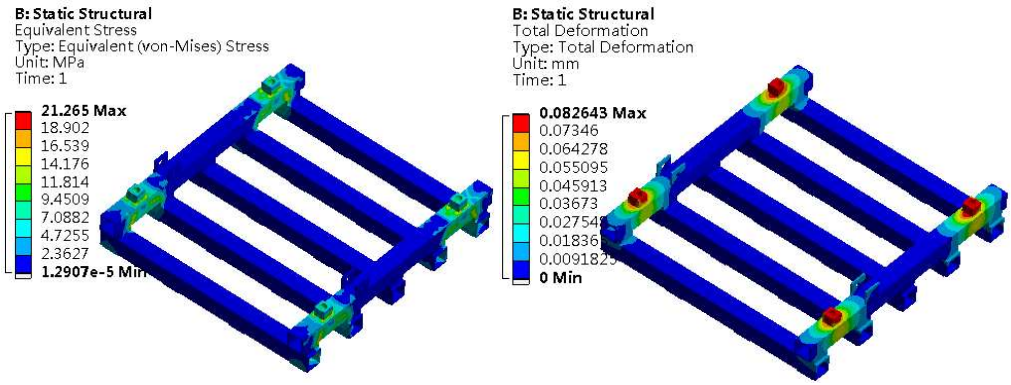

(**a**)

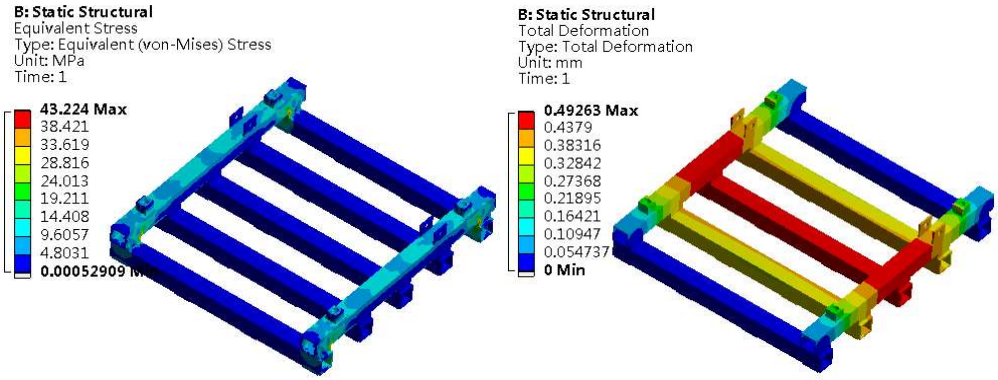

(**b**)

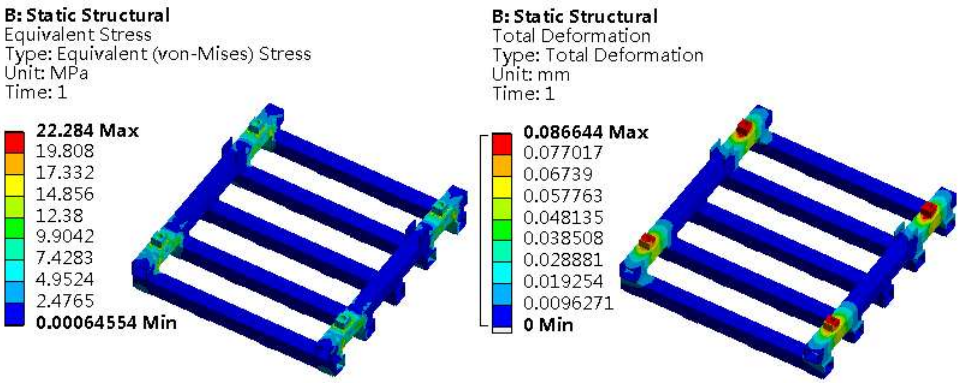

(**c**)

Figure 18. *Cont.*

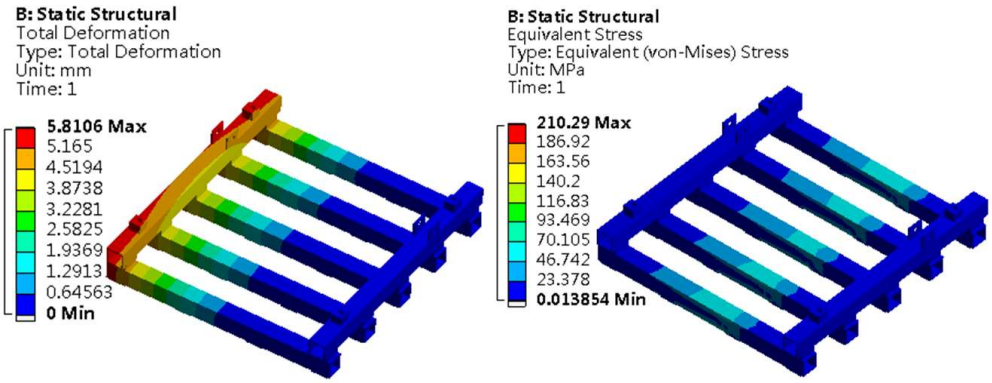

(**d**)

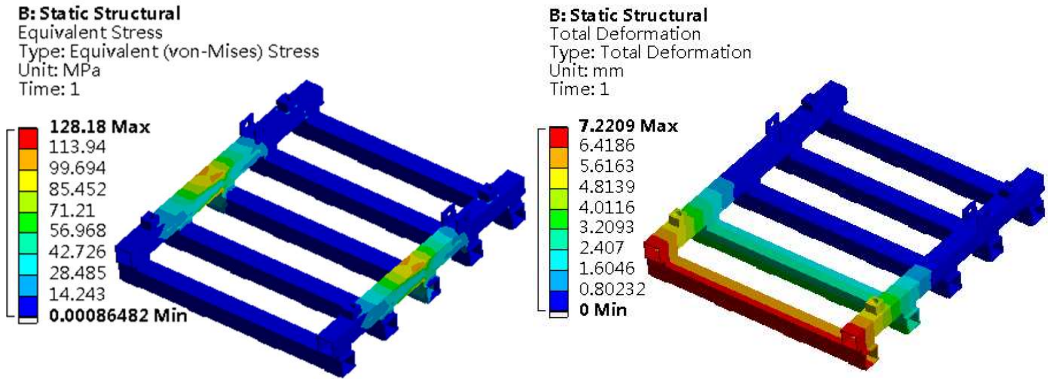

(**e**)

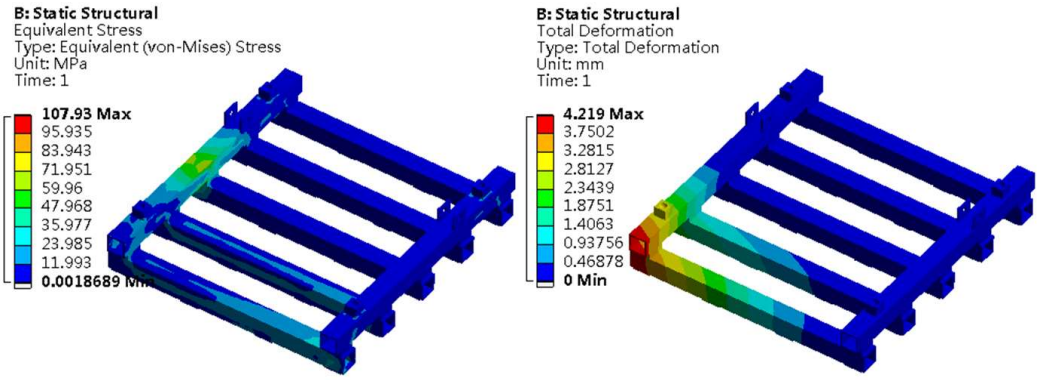

(**f**)

Figure 18. Nephogram of equivalent stress and total deformation. (**a**) Stress and deformation nephogram of main beam under uniform loading; (**b**) stress and deformation nephogram of main beam under loading at both ends; (**c**) stress and deformation nephogram of main beam under loading on both sides; (**d**) stress and deformation nephogram of main beam under lateral eccentric loading; (**e**) stress and deformation nephogram of main beam under longitudinal eccentric loading; (**f**) stress and deformation nephogram of main beam under torsional loading.

Table 5. Maximum stress and deformation of main beam.

Working Condition	Maximum Deformation (mm)	Maximum Stress (MPa)
Working condition 1: uniform loading	0.082	21.26
Working condition 2: loading at both ends	0.492	43.22
Working condition 3: loading on both sides	0.086	22.28
Working condition 4: lateral eccentric load	5.810	210.29
Working condition 5: longitudinal eccentric load	7.220	128.18
Working condition 6: torsional loading	4.219	107.93

(1) The maximum stress of the main beam under each working condition was less than the material yield limit, and the material strength met the requirements.
(2) When the main beam was uniformly loaded, the working condition was the best, the stress under the lateral eccentric load working condition was maximal at 210.29 MPa, and the maximum deformation was 5.81 mm. Under the longitudinal eccentric load condition, the deformation was maximal, and the corresponding maximum stress was 128.18 MPa.
(3) The stress and deformation of the equipment at the forced part and the connection were larger. The reliability of the equipment could be improved by strengthening the part.

4.4.2. Modal Analysis of Main Beam

As the key bearing component of the SmTS, the main beam needs to obtain its natural frequency and mode shape through a modal analysis to determine the reliability of its structural design. In addition to the structure of the main beam itself, the natural frequency of the main beam is also related to the stiffness of the wall rock and other SmTS components. Due to the limitation of our computer's computing ability, the scheme of the main beam modal analysis was simplified. The influence of wall rock and other support components on the natural frequency of the main beam were simplified into load and boundary conditions. Its vibration source was the roadheader, and the external excitation frequency was the vibration frequency generated when the roadheader cut coal and rock. The natural frequency obtained from the modal analysis was compared with this vibration frequency to verify whether the main beam would resonate. The modal analysis of the main beam was conducted through the model module of ANSYS Workbench; the first six natural frequencies of the main beam were obtained as shown in Table 6, and the first six vibration modes are shown in Figure 19.

Table 6. First six natural frequencies of main beam.

No.	Vibration Frequency (Hz)
1	26.41
2	37.16
3	40.77
4	77.06
5	141.92
6	152.40

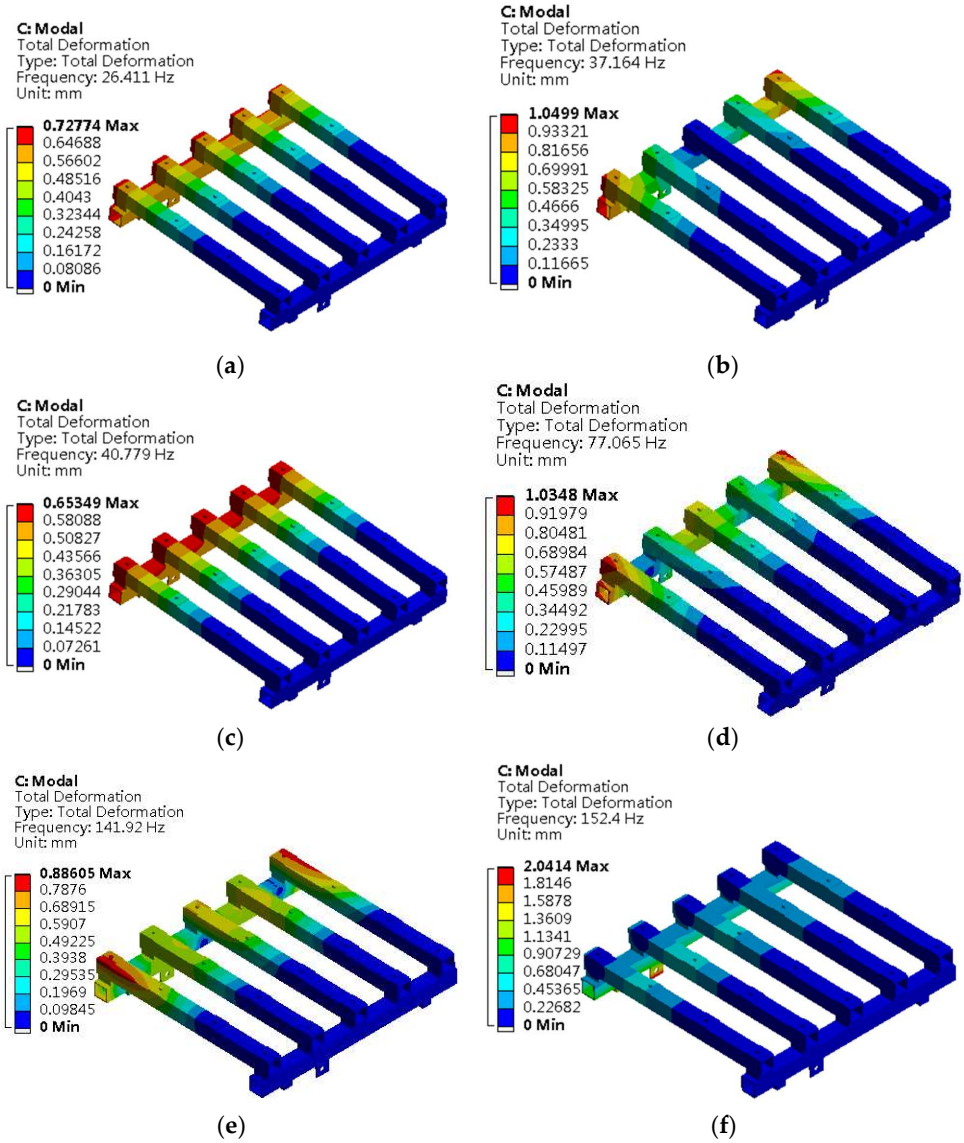

Figure 19. First six vibration modes of main beam. (**a**) First vibration mode, (**b**) second vibration mode, (**c**) third vibration mode, (**d**) fourth vibration mode, (**e**) fifth vibration mode, and (**f**) sixth vibration mode.

According to the first six vibration modes diagram of the main beam, it can be seen that:

(1) The natural frequency of the main beam increased with the increase of the modal order, and the sixth order had the largest natural frequency, which was 152.41 Hz.
(2) The deformation of the main beam at the second-, fourth- and sixth-order modes was larger, and the deformation at the sixth order was the largest, with a maximum relative displacement of 2.04.
(3) The cross bar and longitudinal bar of the main beam were tubular and were prone to bending and breaking. The maximum deformation at the no. 1, no. 3 and no. 6 natural frequencies was located at the end of the longitudinal beam and transverse beam at one side of the main beam, and the maximum deformation at the no. 2, no. 4 and no. 5 natural frequencies was located at the end of the cross beam at both ends.
(4) The working frequency of the roadheader working in parallel with the SmTS was 1.5 Hz. It can be seen from Table 6 that the vibration frequency of each order of the main beam was greatly different from the working frequency of the roadheader, and resonance would not occur.

4.4.3. Fatigue Analysis of Key Components

The fatigue analysis of the main beam was carried out under the condition of a lateral eccentric load. On the basis of the above-mentioned finite element model, the fatigue strength factor was set as 0.7, the load type was zero-based, and the average stress correction criterion was Goodman's. We ran the fatigue analysis module Fatigue Tool in Ansys Workbench to obtain the nephogram of fatigue life, fatigue damage structure, and safety factor, and the fatigue characteristic curve of the main beam, as shown in Figures 20–23, respectively.

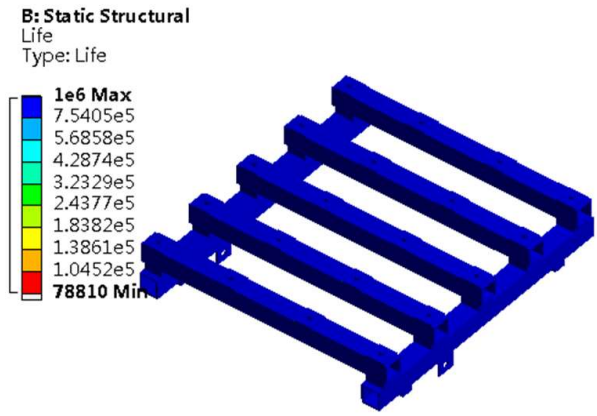

Figure 20. Fatigue life nephogram of main beam.

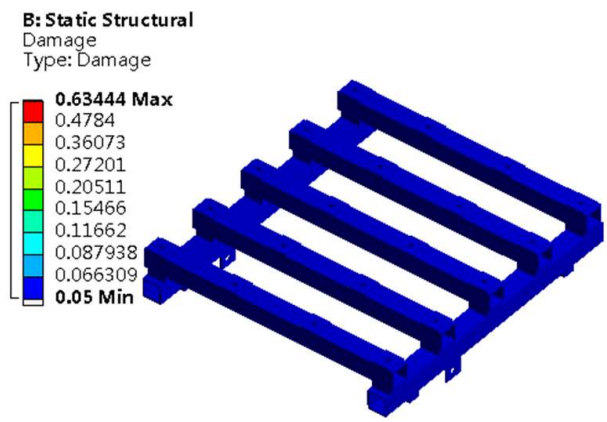

Figure 21. Fatigue damage structural nephogram of main beam.

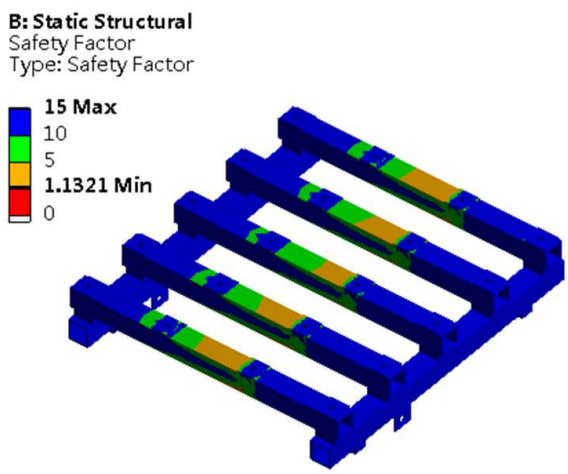

Figure 22. Security factor nephogram of main beam.

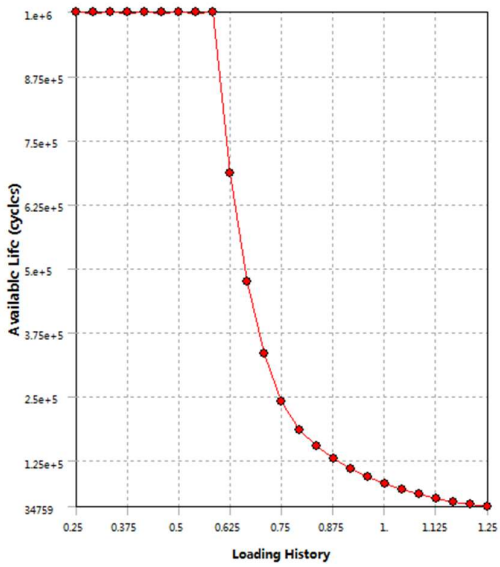

Figure 23. Fatigue sensitivity characteristic curve of main beam.

It can be seen from the fatigue life nephogram of the main beam shown in Figure 20 that the number of cyclic loads in most areas of the main beam was 10^6 times, the lowest fatigue life area was distributed at the connection between the spring support and the beam, and the number of cyclic loads was 78,810 times. The overall strength of the main beam was high, meeting the support requirements. It can be seen from the cloud diagram of the fatigue damage structure shown in Figure 21 that the ratio of the structural design life to the actual life of the main beam was less than 1, indicating that the most vulnerable parts of the main beam could also meet the service requirements.

It can be seen from the safety factor nephogram shown in Figure 22 that the minimum safety factor of the main beam was 1.13, which met the safety requirements. The fatigue sensitivity characteristic curve shown in Figure 23 reflects the sensitivity of fatigue life to load change amplitude. When the basic load change amplitude of the main beam was more than 60%, the fatigue life decreased to 34,759. When the basic load change amplitude was less than 60%, the maximum life value was 10^6. To sum up, the main beam structure was reasonable, and the overall safety met the requirements of working conditions.

5. Multiobjective Optimization of Main Beam Structure Based on RSM

It can be seen from the mechanical characteristics analysis of the support above that the main beam of the support had design redundancy on the premise of meeting the support requirements. In order to optimize the performance of the support and improve the cost performance ratio, a multiobjective optimization method based on RSM was constructed to optimize multiple design parameters of the support main beam.

5.1. Multiobjective Optimization Method Based on RSM

Based on the simulation analysis data of the model, a structural multiobjective optimization method based on RSM [43,44] was proposed. First, we selected the design variables to be optimized, selected the sample points in the design space, and obtained the true response value of the objective function corresponding to the sample points through simulation experiments. Then, the response surface model was determined according to the response value, and the fitting response value of the target function corresponding to the sample point was obtained according to the response surface model. Finally, we verified whether the goodness of fit of the response surface model was reasonable by comparing the real response value with the fitted response value. If it was reasonable, we solved the objective function value iteratively and verified the optimization result, otherwise, we reselected the sample point and calculated again. the process is shown in Figure 24.

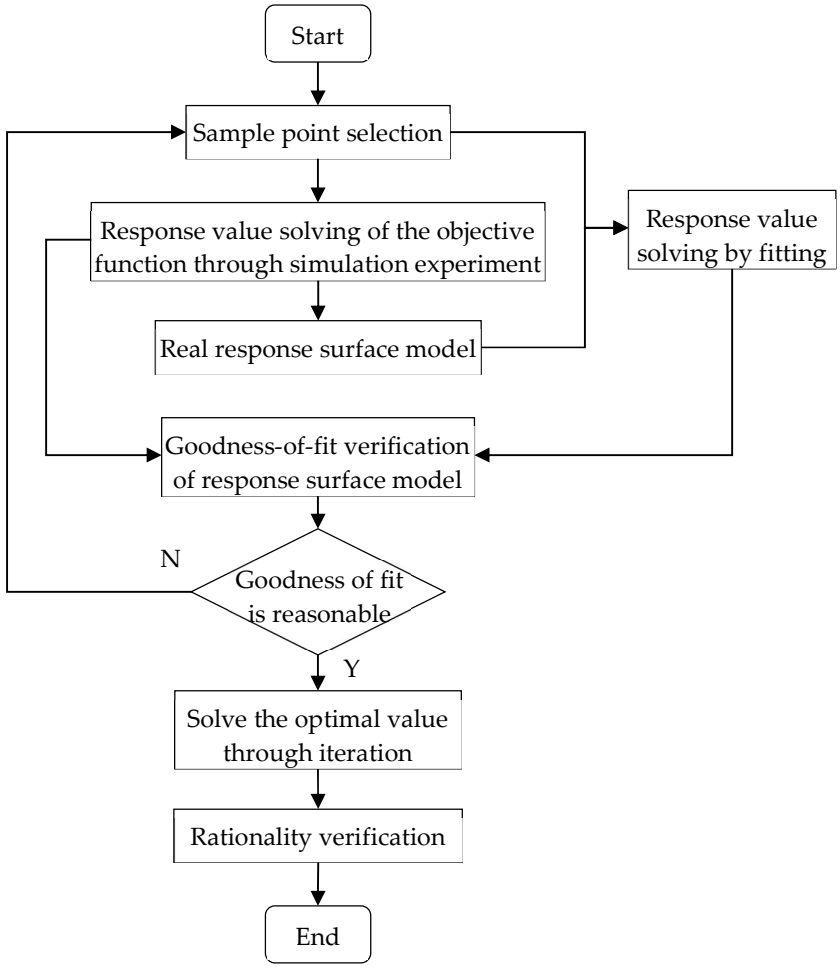

Figure 24. Multiobjective optimization of product structure based on RSM.

The above multiobjective optimization method based on SRM was applied to optimize and solve the model. The main steps were as follows:

(1) Determine the design variables to be optimized in the model and set their value ranges.
(2) Select sample points in the design space and get the true response value of the target function corresponding to the sample points through simulation experiments.
(3) Determine the response surface model according to the sample points and the real response value of the objective function.
(4) Use the response surface model to calculate the fitting response value of the target function corresponding to the sample point.
(5) Verify the goodness of fit of the response surface model by analyzing the true response value and the fitted response value. When the goodness of fit is reasonable, proceed to the next step; otherwise, reselect the sample points or increase the number of sample points, and establish the response surface model again.
(6) Solve the optimal solution of the model objective function iteratively.
(7) Verify the rationality of the optimized design.

5.2. Multiobjective Optimization of Main Beam Structure

Based on the above multiobjective optimization method of the model structure based on RSM, the main beam of SmTS was optimized and improved on the basis of the modeling and analysis in Section 4.

5.2.1. Selection of Optimal Design Variables

Through the analysis in Section 4.4, it can be seen that the stress of the main beam under the lateral eccentric load condition was the largest, and the yield failure was most likely to occur. Therefore, it was necessary to optimize the structure of the main beam under this working condition. The response surface optimization tool provided in the Design Exploration module of ANSYS Workbench was selected as the solution tool. Figure 25 shows the multiobjective optimization module built in ANSYS Workbench.

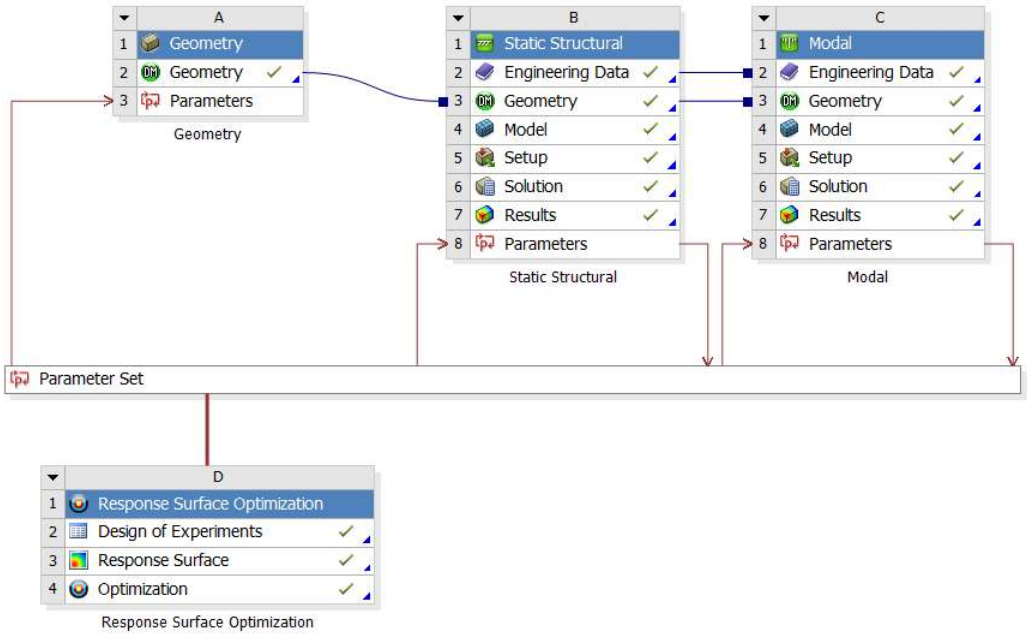

Figure 25. Multiobjective optimization module. (**A**) Set the parameters of "Geomotry", (**B**) Set the parameters of "Static Structural", (**C**) Set the parameters of "Model", (**D**) Set the parameters of "Response Surface Optimization".

The four thickness parameters of the beam in SmTS were selected as design variables, as shown in Figure 26, P1, P2, P3, and P4. The range of value variation was set to be no more than 10% of its initial value. The initial value, upper and lower limit values, and physical meaning of each design variable are shown in Table 7. We imported the model into the analysis software tool to establish the finite element model.

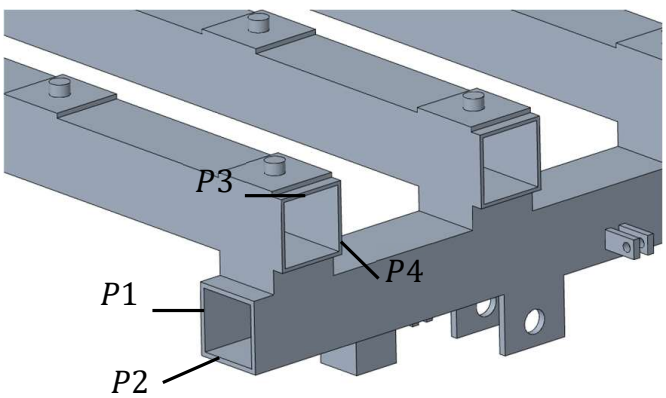

Figure 26. Design variables of main beam.

Table 7. Parameter values of main beam design variables.

Design Variables	Initial Value (mm)	Lower Limit Value (mm)	Upper Limit Value (mm)	Physical Meaning
P1	25.0	22.5	27.5	Thickness of left and right walls of longitudinal beam
P2	25.0	22.5	27.5	Thickness of upper and lower walls of longitudinal beam
P3	30.0	27.0	33.0	Thickness of left and right walls of cross beam
P4	30.0	27.0	33.0	Thickness of upper and lower walls of cross beam

5.2.2. Selection of Sample Points and Calculation of Real Response Value

Four design variables with a certain value range together constituted the design space, which contained a large number of design variables with different permutations and combinations. A group of sample points were selected in the design space through the experimental design method, and the structure was optimized based on the sample points. Whether the sample points were selected reasonably affected the accuracy of the analysis results.

The central composite design (CCD) was adopted to select the sample points. The CCD sample points were composed of cubic points, axial points, and central points [45]. The number of sample points n_c was as follows

$$n_c = 2^{n_s - \zeta} + 2n_s + 1 \tag{22}$$

where n_c is the number of sample points, ζ is the factorial coefficient, and n_s is the number of design variables. Among them, the factorial coefficient corresponding to the number of design variables and the number of sample points are shown in Table 8.

Table 8. Number of central composite test design sample points.

n_s	ζ	n_c
1	0	5
2	0	9
3	0	15
4	0	25
5	1	27
6	1	45

There were four design variables in the optimal design of the main beam. According to Table 8, the factorial coefficient was 0 and the number of sample points was 25. Some sample points generated through the central composite design in ANSYS Workbench are shown in Table 9.

The true response values of the objective functions, such as the maximum deformation and maximum equivalent stress of the main beam corresponding to each sample point in Table 9, are shown in Table 10.

Table 9. Sample points selected for central composite design.

No.	P1 (mm)	P2 (mm)	P3 (mm)	P4 (mm)
1	25.0	25.0	30.0	30.0
2	22.5	25.0	30.0	30.0
3	27.5	25.0	30.0	30.0
4	25.0	22.5	30.0	30.0
5	25.0	27.5	30.0	30.0
6	25.0	25.0	27.0	30.0
7	25.0	25.0	23.0	30.0
8	25.0	25.0	30.0	27.0
...	...	...	...	...
14	23.239	23.239	32.113	27.887
15	26.760	23.239	32.112	27.887
16	23.239	26.760	32.112	27.887
17	26.760	26.760	32.112	27.887
18	23.239	23.239	27.887	32.112
19	26.760	23.239	27.887	32.112
20	23.239	26.760	27.887	32.112
21	26.760	26.760	27.887	32.112
22	23.239	23.239	32.112	32.112
23	26.760	23.239	32.112	32.112
24	23.239	26.760	32.112	32.112
25	26.760	26.760	32.112	32.112

Table 10. True response value of sample point objective function.

No.	Max. Deformation (mm)	Max. Equivalent Stress (MPa)	Minimum Fatigue Life (Times)	First Order Natural Frequency (Hz)	Quality (kg)
1	5.810	210.288	78,810.001	26.411	8436.186
2	5.819	210.492	78,633.709	26.644	8347.873
3	5.801	209.859	79,507.420	26.185	8524.498
4	5.815	211.099	77,807.800	26.643	8347.873
5	5.811	210.280	78,925.294	26.184	8524.498
6	6.108	221.705	65,001.531	25.993	8204.454
7	5.587	205.360	86,086.919	26.741	8667.918
8	5.984	243.385	46,162.493	26.237	8204.454
...	...	...	...	...	...
14	5.766	238.070	50,057.375	26.861	8313.802
15	5.753	237.370	50,600.337	25.938	8439.934
16	5.764	237.765	50,292.723	25.940	8439.933
17	5.747	237.277	50,672.835	25.624	8562.561
18	5.932	219.041	67,949.483	26.861	8313.806
19	5.911	217.810	69,368.278	26.521	8439.938
20	5.920	219.261	67,699.881	26.520	8439.937
21	5.908	212.324	76,174.330	26.209	8562.565
22	5.576	206.510	84,341.098	26.519	8634.433
23	5.555	206.278	84,689.830	26.183	8760.565
24	5.561	207.553	82,797.412	26.188	8760.564
25	5.552	206.538	84,298.557	25.881	8883.192

5.2.3. Construction of Response Surface Model for Multiobjective Optimization of Main Beam

According to the above optimization variables and model optimization requirements, the mathematical model of design variables, objective functions, and constraints was constructed, and the response surface model was built and solved.

The mathematical representation of the design variables was as follows

$$X = [x_1, x_2, x_3, x_4]^\top \tag{23}$$

where x_i represents the no. i design variable, $i = 1,\ 2,\ 3,\ 4$, corresponding to the parameter $P_1 - P_4$ of the main beam.

The value range of design variables was expressed as:

$$u_i \leq x_i \leq v_i,\ i = 1,\ 2,\ 3,\ 4 \tag{24}$$

where u_i and v_i represent the lower and upper limit values of design variables, respectively, and their specific values are shown in Table 7.

The optimization aimed to minimize the mass, equivalent stress, deformation, first-order natural frequency, and minimum fatigue life of the main beam. Its objective function was defined as

$$\begin{cases} f_1(x_i) = \min S(x_i)(i = 1,2,3,4) \\ f_2(x_i) = \min M(x_i)(i = 1,2,3,4) \\ f_3(x_i) = \min D(x_i)(i = 1,2,3,4) \\ f_4(x_i) = \max F(x_i)(i = 1,2,3,4) \\ f_5(x_i) = \max L(x_i)(i = 1,2,3,4) \end{cases} \tag{25}$$

where $S(x_i)$ is the maximum equivalent stress of the main beam, $M(x_i)$ is the mass of the main beam, $D(x_i)$ is the maximum deformation of the main beam, $F(x_i)$ is the first-order natural frequency of the main beam, and $L(x_i)$ is the minimum service life of the main beam.

The maximum equivalent stress of the main beam was less than the allowable stress of the material, so the constraint condition was expressed as

$$\sigma(x_i) \leq [\sigma], i = 1,2,3,4 \tag{26}$$

where $\sigma(x_i)$ is the maximum equivalent stress of main beam and $[\sigma]$ is the allowable stress of material.

According to the above definition of the design variables, constraints and objective functions, the multiobjective optimization mathematical model of the main beam can be expressed as:

$$\begin{cases} x = [x_1, x_2, x_3, x_4]^\top \\ f_1(x_i) = \min S(x_i) \\ f_2(x_i) = \min M(x_i) \\ f_3(x_i) = \min D(x_i) \\ f_4(x_i) = \max F(x_i) \\ f_5(x_i) = \max L(x_i) \\ u_i \leq x_i \leq v_i (i = 1,2,3,4) \\ \sigma(x_i) \leq [\sigma] \end{cases} \tag{27}$$

The response surface model represents the functional relationship between the sample point and its target function response value. Its general formula is shown as follows

$$y = \beta_0 + \sum_{i=1}^{n} \beta_i x_i + \sum_{i=2}^{n} \sum_{j=1}^{i-1} \beta_{ij} x_i x_j + \sum_{i=1}^{n} \beta_{ii} x_i^2 + \varepsilon \tag{28}$$

where y is the objective function, β is the regression equation coefficient, x_i is the design variable, n is the number of design variables, and ε is the error term.

In the multiobjective optimization of the main beam, the response outputs of the design variables x_1, x_2, x_3, and x_4 were, respectively, the maximum deformation $D(x)$, the maximum equivalent stress $S(x)$, the minimum fatigue life $L(x)$, the first-order natural frequency $F(x)$, and the mass $M(x)$ of the main beam. Therefore, the test had four factors and five responses, and the response surface model was

$$\begin{aligned} y(x) = \beta_0 + \beta_1 x_1 + \beta_2 x_2 + \beta_3 x_3 + \beta_4 x_4 + \beta_{11} x_1^2 + \beta_{11} x_1^2 + \beta_{22} x_2^2 + \beta_{33} x_3^2 + \beta_{44} x_4^2 + \beta_{12} x_1 x_2 + \beta_{13} x_1 x_3 \\ + \beta_{14} x_1 x_4 + \beta_{23} x_2 x_3 + \beta_{24} x_2 x_4 + \beta_{34} x_3 x_4 + \varepsilon \end{aligned} \tag{29}$$

The above formula can be expressed in matrix as follows

$$y(x) = \alpha^T \beta + \varepsilon \tag{30}$$

where the definition of α and β are as follows

$$\alpha = [1, x_1, x_2, x_3, \ldots, x_3 x_4] \tag{31}$$

$$\beta = [\beta_0, \beta_1, \beta_2, \beta_3, \ldots, \beta_{34}]^T \tag{32}$$

When there is k groups of tests, Formula (30) is expressed as follows

$$Y = X \cdot B + \varepsilon \tag{33}$$

In Formula (33), matrix B is an unknown matrix representing the relationship between an independent variable and a dependent variable. The unknown matrix B [46] was calculated by the least square method, and its calculation formula was as follows

$$B = \left(X^T X\right)^{-1} X^T Y \tag{34}$$

The response surface models of the maximum deformation $D(x)$, the maximum equivalent stress $S(x)$, the minimum fatigue life $L(x)$, the first-order natural frequency $F(x)$, and the mass $M(x)$ of the main beam were obtained by calculating the data of sample points and their response values in Tables 9 and 10 using the above method, as shown in Formulas (35), (36), (37), (38), and (39), respectively.

$$\begin{aligned} D(x) = 22.88 - \; & 8.14 \times 10^2 x_1 - 9.91 \times 10^2 x_2 - 0.505 x_3 - 0.33 x_4 + 4.03 \times 10^4 x_2 - 2.34 \times 10^{-17} x_1 x_3 \\ & -2.79 \times 10^{-17} x_1 x_4 - 3.36 \times 10^4 x_2 x_3 - 3.36 \times 10^4 x_2 x_4 - 3.36 \times 10^4 x_3 x_4 + 1.34 \times 10^3 x_1^2 \\ & +2.14 \times 10^3 x_2^2 + 5.37 \times 10^3 x_3^2 + 3.15 \times 10^3 x_4^2 \end{aligned} \tag{35}$$

$$\begin{aligned} S(x) = 6.06 \times 10^3 - \; & 42.01 x_1 - 47.26 x_2 - 89.52 x_3 - 2.14 \times 10^2 x_4 - 0.12 x_1 x_2 + 0.11 x_1 x_3 - 0.11 x_1 x_4 \\ & +0.11 x_2 x_3 - 5.91 \times 10^{-2} x_2 x_4 + 0.68 x_3 x_4 + 0.89 x_1^2 + 0.97 x_2^2 + 0.99 x_3^2 + 31.82 x_4^2 \end{aligned} \tag{36}$$

$$\begin{aligned} L(x) = -4.57 \times 10^6 + \; & 2.59 \times 10^4 x_1 + 3.45 \times 10^4 x_2 + 6.02 \times 10^4 x_3 + 1.88 \times 10^5 x_4 + 1.62 \times 10^2 x_1 x_2 \\ & -1.31 \times 10^2 x_1 x_3 + 1.71 \times 10^2 x_1 x_4 - 1.38 \times 10^2 x_2 x_3 + 71.96 x_2 x_4 - 31.35 x_3 x_4 \\ & -6.16 \times 10^2 x_1^2 - 7.29 \times 10^2 x_2^2 - 8.19 \times 10^2 x_3^2 - 3.11 \times 10^3 x_4^2 \end{aligned} \tag{37}$$

$$\begin{aligned} F(x) = 7.62 - \; & 1.79 \times 10^{-2} x_1 + 2.21 \times 10^{-2} x_2 + 0.67 x_3 + 0.54 x_4 + 1.81 \times 10^{-3} x_1 x_2 + 1.68 \times 10^{-4} x_1 x_3 \\ & +1.68 \times 10^{-4} x_1 x_4 - -1.68 \times 10^{-4} x_2 x_3 + 5.01 \times 10^{-4} x_2 x_4 - 3.51 \times 10^{-3} x_3 x_4 \\ & -2.58 \times 10^{-3} x_1^2 - 3.38 \times 10^{-3} x_2^2 - 7.34 \times 10^{-3} x_3^2 - 6.79 \times 10^{-3} x_4^2 \end{aligned} \tag{38}$$

$$\begin{aligned} M(x) = 1.27 \times 10^3 + \; & 42.4 + 42.4 x_2 + 96.69 x_3 + 96.7 x_4 - 0.28 x_1 x_2 - 1 \times 10^{-13} x_1 x_3 - 9.27 \times 10^{-15} x_1 x_4 \\ & +1.35 \times 10^{-13} x_2 x_3 + 4.49 \times 10^{-14} x_2 x_4 - 0.64 x_3 x_4 - 1.63 \times 10^{-7} x_1^2 - 1.63 \times 10^{-7} x_2^2 \\ & -1.13 \times 10^{-7} x_3^2 - 1.13 \times 10^{-7} x_4^2 \end{aligned} \tag{39}$$

5.2.4. Fitting Response Value Solution and Goodness-Of-Fit Analysis

We calculated the values of Formulas (35)–(39) to obtain the fitting response values of the corresponding objective functions such as the maximum deformation, maximum equivalent stress, and minimum fatigue life of the main beam at each sample point, as shown in Table 11.

Table 11. Sample point objective function fitting response value.

No.	Max. Deformation (mm)	Max. Equivalent Stress (MPa)	Min. Fatigue Life (Times)	First-Order Natural Frequency (Hz)	Mass (kg)
1	5.803	205.732	82,113.190	26.426	8436.186
2	5.822	212.233	77,230.004	26.639	8347.852
3	5.801	210.420	79,294.534	26.181	8524.519
4	5.821	212.238	77,093.582	26.634	8347.852
5	5.811	211.445	78,022.916	26.177	8524.519
6	6.122	225.696	64,658.508	25.970	8204.226
7	5.580	203.672	84,816.411	26.750	8668.145
8	5.989	257.428	33,054.988	26.215	8204.220
9	5.673	211.320	75,044.701	26.516	8668.151
10	6.178	257.849	37,772.533	26.280	7981.767
...	...	...	...	...	...
14	5.769	234.588	54,228.663	26.859	8313.807
15	5.752	235.838	52,435.727	26.526	8439.930
16	5.760	236.030	52,316.939	26.521	8439.930
17	5.747	235.718	52,531.648	26.210	8562.554
18	5.928	220.614	65,779.008	26.517	8313.815
19	5.911	218.374	68,471.157	26.184	8439.938
20	5.918	219.617	66,991.589	26.189	8439.938
21	5.906	215.814	71,691.383	25.878	8562.562
22	5.580	209.575	81,676.828	27.034	8634.355
23	5.562	209.092	82,425.723	26.703	8760.478
24	5.566	210.140	80,834.164	26.704	8760.478
25	5.553	208.095	83,590.704	26.395	8883.102

Because there was a deviation between the predicted value of the response surface model and the true response value, only the approximate solution of the objective function could be obtained. To ensure the accuracy of the predicted data of the response surface model, its goodness of fit was verified through a significance analysis. The prediction ability of the response surface model could be determined according to the decision coefficient R^2, the modified decision coefficient R_a^2, and the normalized root-mean-square difference $NRMSD$. The closer the decision coefficient R^2 and the modified decision coefficient R_a^2 were to 1, and the closer the normalized root-mean-square difference $NRMSD$ was to 0, the better the significance of the response surface model was, and the more accurate the predictive value was.

The determination coefficient R^2 is defined as follows

$$R^2 = 1 - \frac{SSE}{SST} \tag{40}$$

where SSE is the sum of residual squares, SST is the sum of total squares, and they are defined as follows, respectively,

$$SST = \sum_{i=1}^{n} (y_i - \overline{y})^2 \tag{41}$$

$$SSE = \sum_{i=1}^{N} (y_i - \hat{y}_i)^2 \tag{42}$$

where y_i is the true response value of sample point, $\overline{y}$ is the average value of the real point response value of the sample, $\hat{y}_i$ is the sample point fitting response value, and n is the number of sample point response values.

The corrected decision coefficient R_a^2 is defined as follows

$$R_a^2 = 1 - \frac{SSE(n-1)}{SST(n-n_s-1)} \tag{43}$$

where n_s is the number of design variables.

The normalized root-mean-square difference $NRMSD$ is defined as follows

$$NRMSD = \frac{\sqrt{\frac{1}{n}\sum_{i=1}^{n}(y_i - \hat{y}_i)^2}}{\frac{1}{n}\sum_{i=1}^{n} y_i} \tag{44}$$

The significance analysis parameters of the response surface model calculated according to Formulas (40)–(44) are shown in Table 12. R^2 and R_a^2 of each objective function were close to 1, and $NRMSD$ was close to 0, which indicated that the data had good significance, that is, the goodness of fit of the response surface model was good.

Table 12. Response surface model significance analysis parameters.

Fit Goodness Index	$D(x)$	$S(x)$	L	$F(x)$	$M(x)$
R^2	0.999	0.946	0.945	0.999	0.999
R_a^2	0.999	0.935	0.934	0.999	0.999
$NRMSD$	8.58×10^{-4}	8.63×10^{-4}	3.00×10^{-6}	7.58×10^{-3}	2.37×10^{-5}

The goodness of fit of the response surface model obtained through ANSYS Workbench is shown in Figure 27. The test points of the objective function in the figure were all distributed on the fitting curve, which further showed that the response surface model had a good fit.

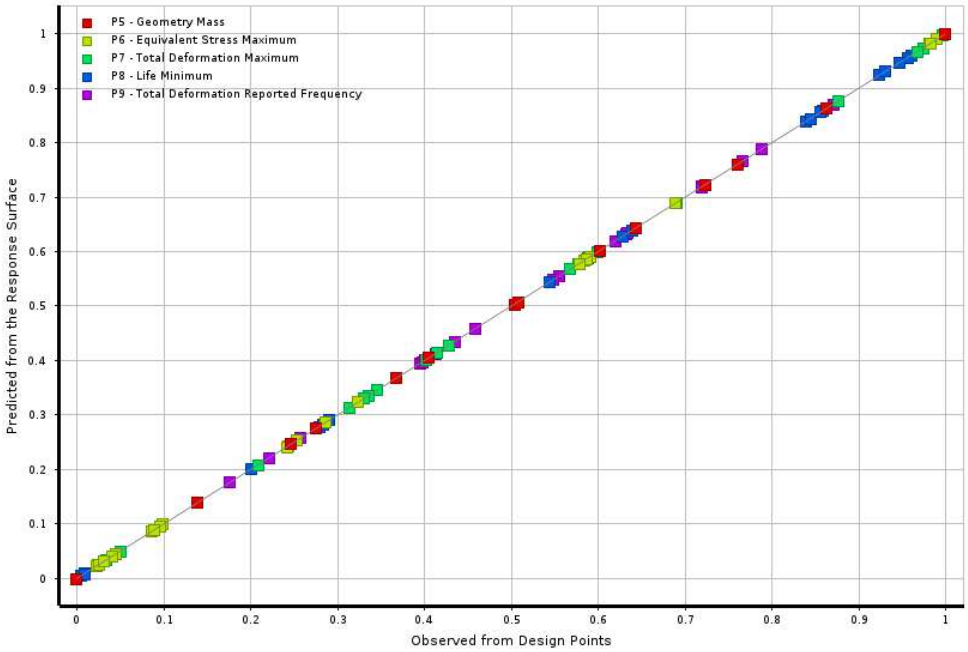

Figure 27. Fitting degree of test factors to objective function.

5.2.5. Response Surface Analysis

The response surface graph can directly reflect the influence of design variables on the objective function. According to the response surface graph, the influence of the design variables on the objective function can be determined, and the response surface graph can be obtained through the multiobjective optimization module of ANSYS Workbench. Taking the design variables P3 and P4 of the main beam as an example, the response surface of P3 and P4 to the mass, maximum deformation, maximum stress, first-order natural frequency, and fatigue life of the main beam were obtained, as shown in Figures 28–32, respectively.

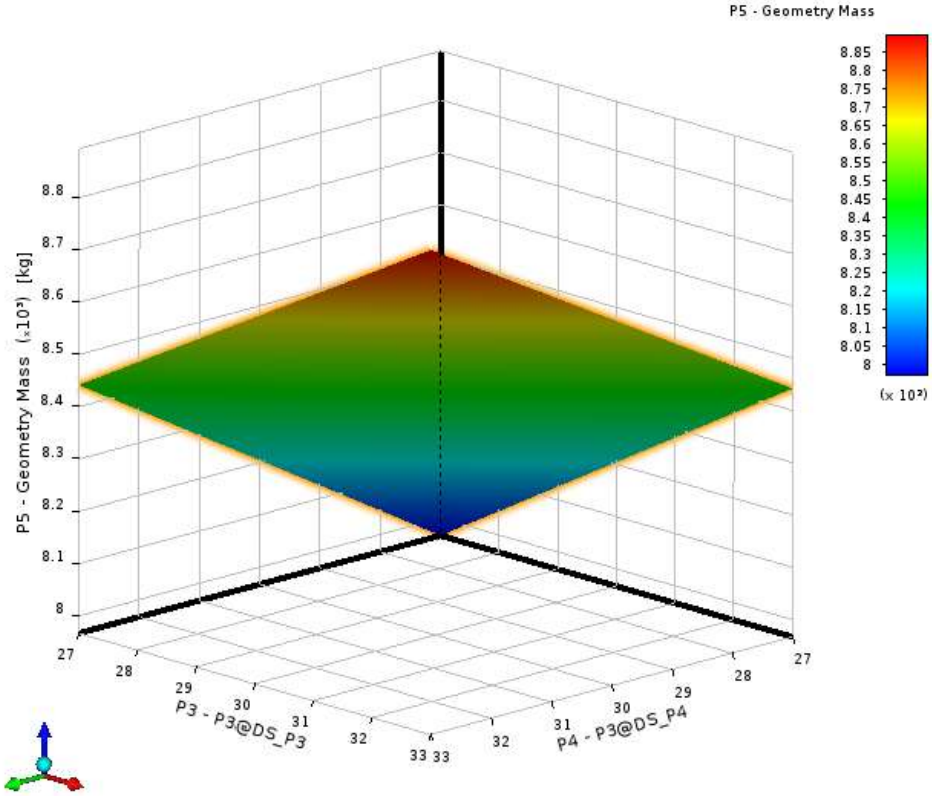

Figure 28. Quality response surface.

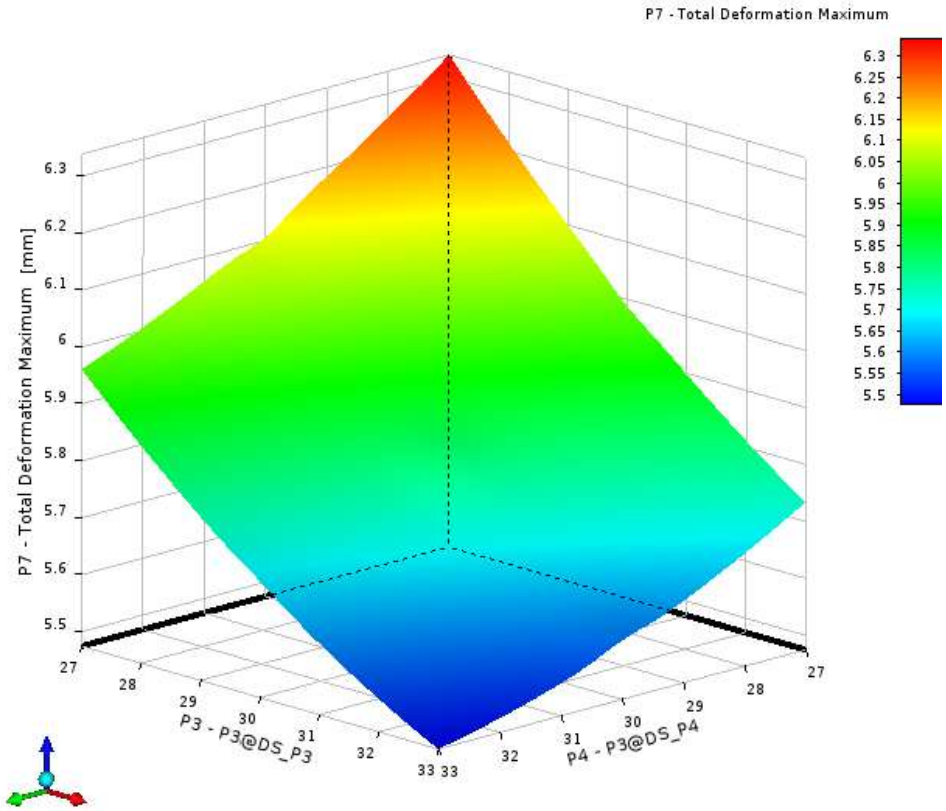

Figure 29. Deformation response surface.

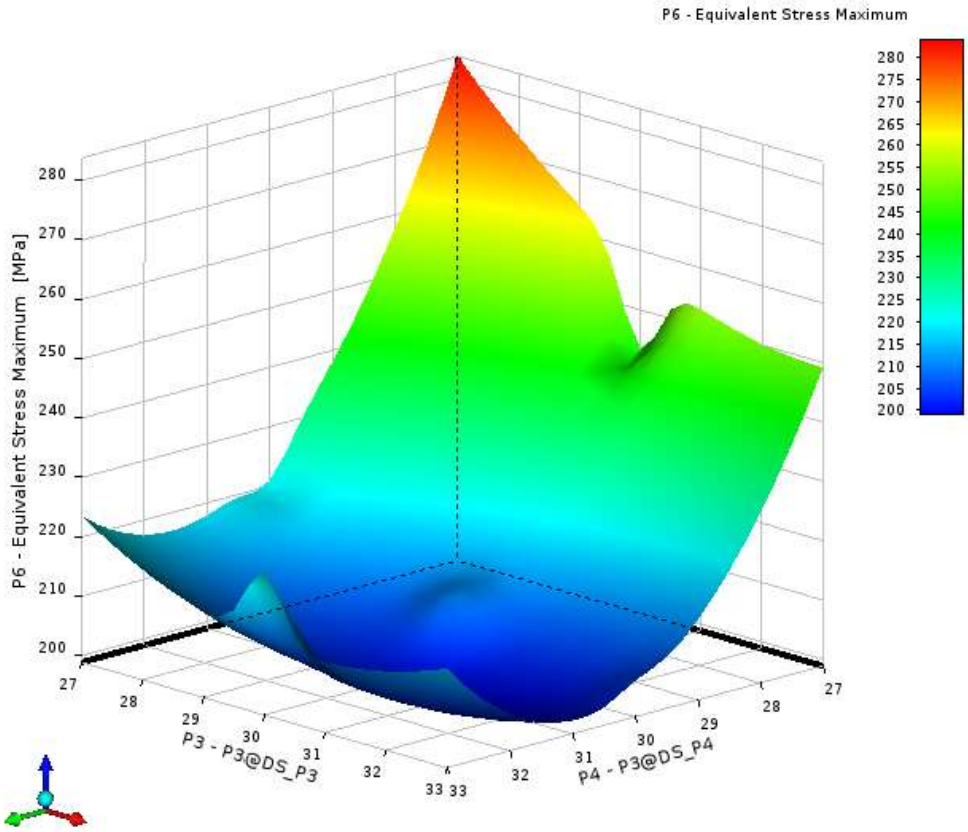

Figure 30. Equivalent stress response surface.

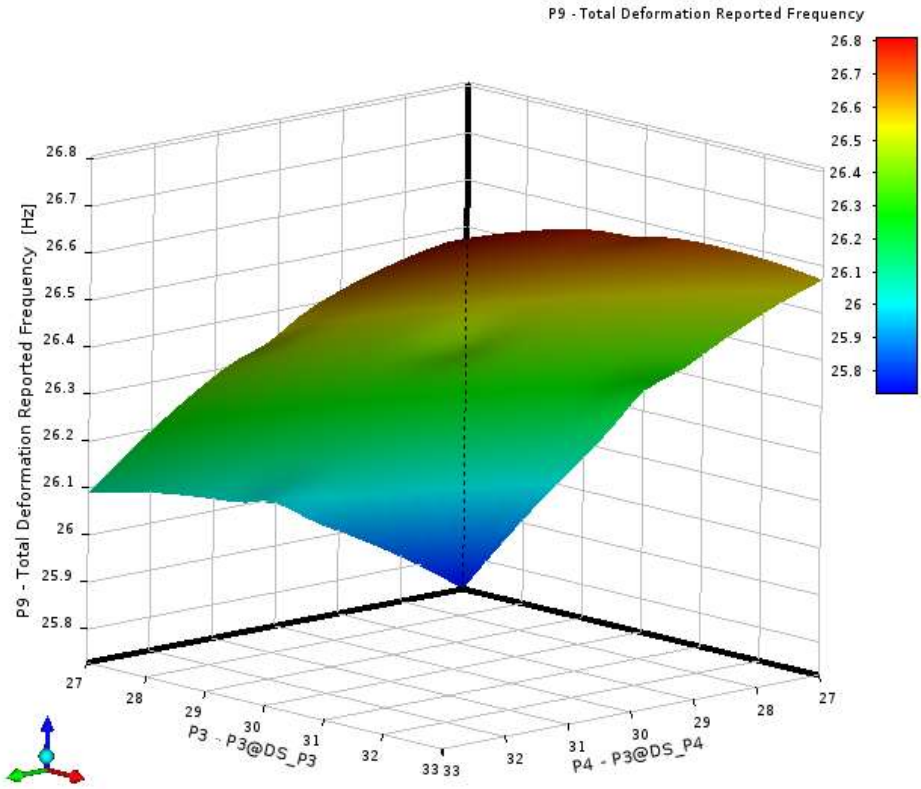

Figure 31. First order natural frequency response surface.

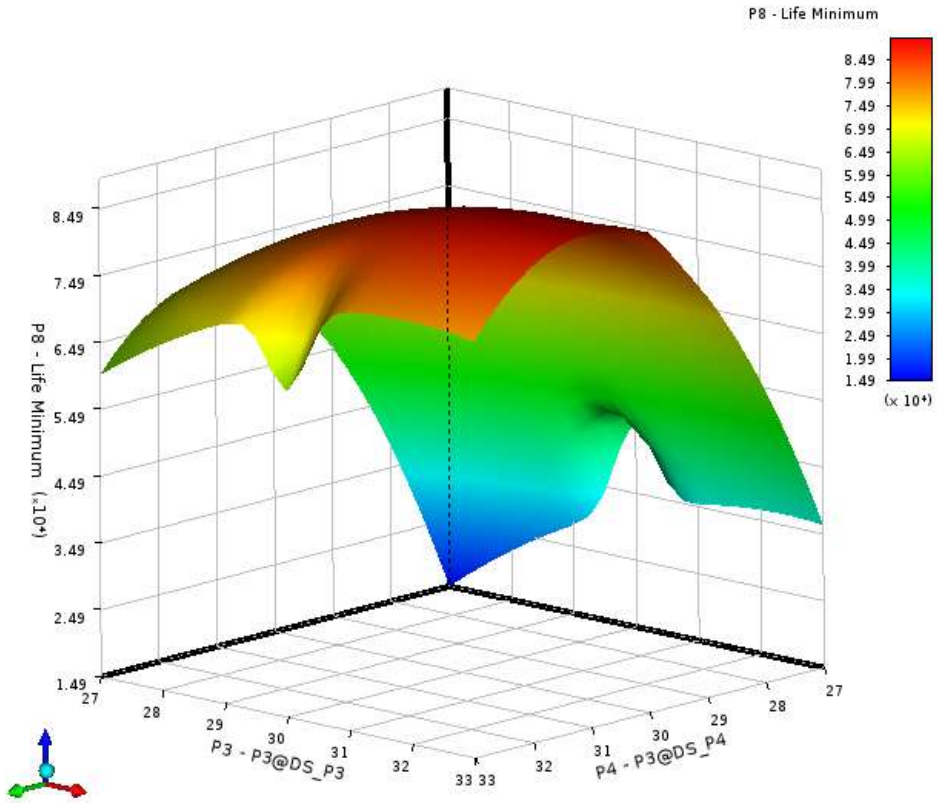

Figure 32. Fatigue life response surface.

It can be seen from the above response surface diagram that with the increase of P3 and P4, the weight of the main beam increased, the maximum deformation decreased, the maximum stress decreased, the first natural frequency increased, and the fatigue life increased. The influence of the above design variables on the objective function provided a basis for the subsequent correction of the design variables and determination of the optimal design scheme.

5.2.6. Multiobjective Optimization Solution of Main Beam

Generally, it is difficult for multiple objective functions to obtain the optimal solution at the same time. When one optimization objective reaches the optimal value, the other optimization objectives are not optimal. Therefore, a large number of effective solutions, namely Pareto solutions [47], re obtained in the multiobjective optimization problem. The goal of multiobjective optimization is to obtain multiple Pareto solutions and select the optimal solution from the Pareto solution set according to the actual demand.

In this paper, the multiobjective genetic algorithm [48] in the optimization module of ANSYS Workbench was used to iteratively solve the response surface model established above, and the Pareto solution set was obtained after. The multiobjective optimization design of the main beam included four design variables and five objective functions, which belonged to the multivariable multiobjective optimization problem and a multiobjective genetic algorithm was applicable.

In order to improve material utilization and reduce the maximum equivalent stress of the main beam, the maximum equivalent stress and mass of the main beam were set as the highest priority before the iterative solution. The multiobjective genetic algorithm was selected as the solution method. The initial population size, iteration number, and other parameters were set and solved iteratively. The three groups of optimal solutions are shown in Table 13. The optimal design scheme was determined from the three groups of solutions.

Table 13. Optimal solution of multiobjective optimization.

No.	P1 (mm)	P2 (mm)	P3 (mm)	P4 (mm)	Max. Deform. (mm)	Max. Stress (MPa)	Min. Fatigue Life (Times)	1st Order Frequency (Hz)	Mass (kg)
1	22.96	23.63	31.25	30.26	5.706	206.84	82566	26.89	8432.2
2	23.86	22.66	31.08	30.38	5.714	207.33	82152	26.88	8426.0
3	24.86	23.04	30.09	30.52	5.778	206.35	82042	26.64	8410.9

Comparing the three groups of optimization schemes in Table 13, in order to reduce the maximum equivalent stress and mass of the main beam as much as possible, the third group of schemes was selected, and its design variables were rounded. The final correction values of each design variable are shown in Table 14.

Table 14. Design variable correction value.

Design Variables	Original Value (mm)	Optimization Value (mm)	Correction Value (mm)
P1	25	24.86	24.9
P2	25	23.04	23.0
P3	30	30.09	30.1
P4	30	30.52	30.5

5.3. Verification of Main Beam Optimization

According to the values of the design variables in Table 14, the main beam was simulated and analyzed under the condition of a lateral eccentric loading. The optimized stress nephogram, deformation nephogram, fatigue life nephogram, and first-order natural frequency nephogram are shown in Figures 33–36, respectively. By comparing Figure 18d, Figure 19a, and Figure 20 before optimization, it can be seen that after optimization, the maximum stress of the main beam decreased to 206.82 MPa, the maximum deformation decreased to 5.78 mm, the first natural frequency was adjusted to 26.72 Hz, and the fatigue life increased to 82769 times. Through measurement, it can be seen that the mass of the main beam decreased to 8419.1 kg.

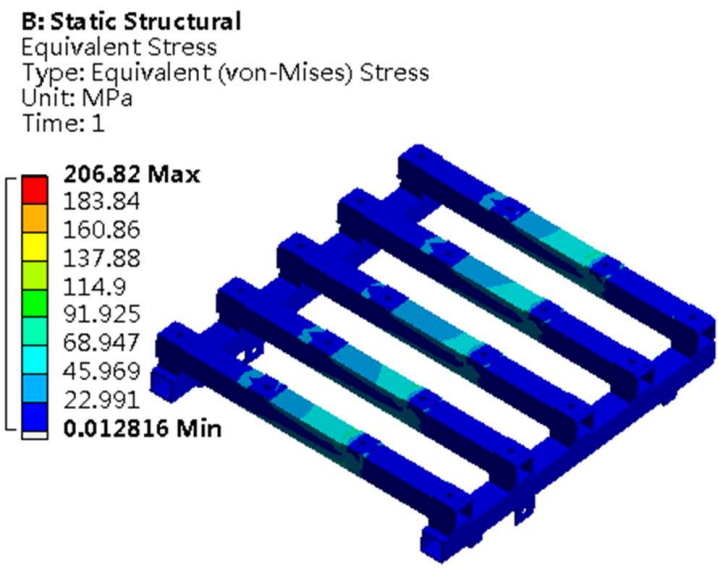

Figure 33. Stress nephogram of main beam.

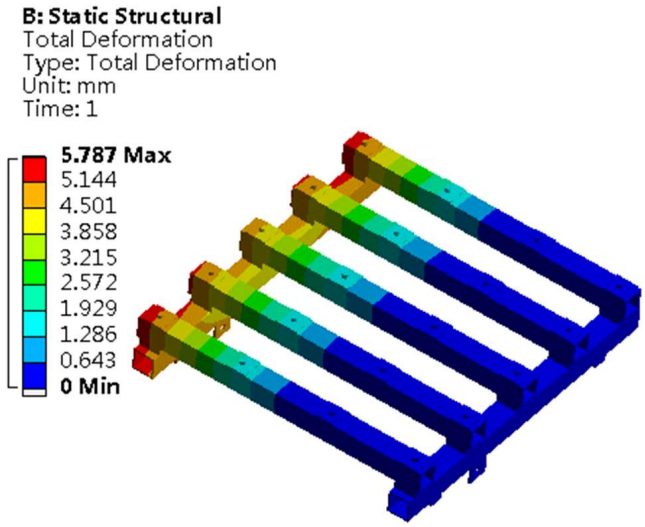

Figure 34. Deformation nephogram of main beam.

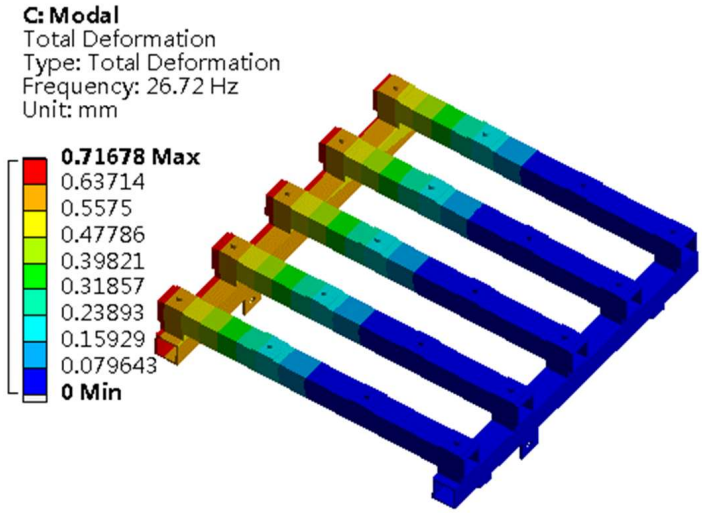

Figure 35. First-order natural frequency nephogram of main beam.

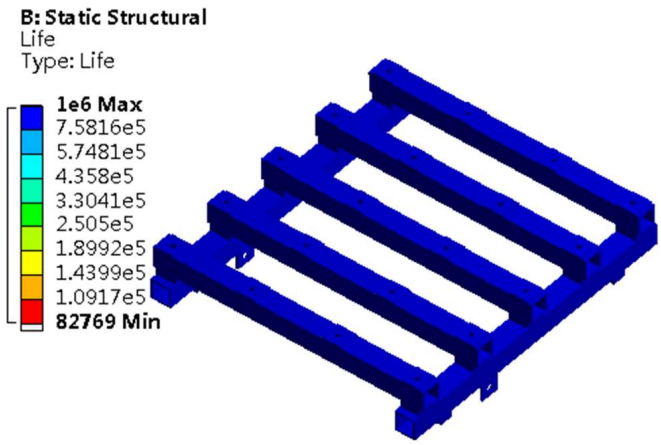

Figure 36. Fatigue life nephogram of main beam after optimization.

The performance parameters of the main beam before and after optimization are shown in Table 15. After optimization, the quality and maximum equivalent stress of the main beam were reduced, and other properties were also optimized, which showed that

the overall performance of the main beam was improved and verified the rationality of the structural optimization of the main beam.

Table 15. Performance parameters of main beam before and after optimization.

Index	Max. Deformation (mm)	Max. Stress (MPa)	Min. Fatigue Life (Times)	First-Order Natural Frequency (Hz)	Mass (kg)
Before optimization	5.81	210.29	78810	26.41	8516.2
After optimization	5.78	206.82	82769	26.72	8419.1
Variation (%)	−0.51%	−1.65%	+5.02%	+1.17%	−1.14%

6. Conclusions

In summary, aiming at the temporary support problem of the coal mine roadway heading face, we proposed a temporary support scheme that could adapt to the uneven roof of the roadway, we analyzed and optimized the scheme and its equipment, and we solved the problem of efficient temporary support under the complex geological conditions of the roadway heading face under the condition of ensuring the cooperative operation of multiple pieces of equipment on site. Firstly, the mechanical characteristics of the wall rock support system in the coal mine roadway were analyzed, which provided a data premise for the temporary support scheme. Then, a novel self-moving temporary support scheme and its equipment were proposed, and the static, modal, and fatigue finite element simulation of its structure were carried out to verify its safety. Finally, a multiobjective optimization method based on RSM was proposed to solve the problem of the design redundancy of the support. The key components of the support were optimized, and the optimization results were verified.

Compared with previous research, our research solved the temporary support problem of a roadway heading face under complex geological conditions. The application of our research can realize the cooperative work of SmTS and other equipment in the coal mine roadway heading face and improve the roadway heading efficiency.

Our future work will focus on installing loads such as a roof bolter on the SmTS, realizing the cooperation with the permanent support. In addition, the support prototype needs to be applied in more coal mines to achieve further verification.

Author Contributions: S.D. has made contributions to the conceptualization, investigation, and original draft writing. J.B. contributed to the validation and resource. J.H. contributed to the methodology and resource. H.W. contributed to methodology, software, and validation. F.M. contributed to methodology and draft review and editing. All authors have read and agreed to the published version of the manuscript.

Funding: This research was funded by the National Natural Science Foundation of China (Grant no. 52005302 and no. 52105463).

Institutional Review Board Statement: Not applicable.

Informed Consent Statement: Not applicable.

Data Availability Statement: Not applicable.

Conflicts of Interest: The authors declare no conflict of interest.

References

1. Wang, C.L.; Liu, L.; Elmo, D.; Shi, F.; Gao, A.S.; Ni, P.P.; Zhang, B.C. Improved energy balance theory applied to roadway support design in deep mining. *J. Geophys. Eng.* **2018**, *15*, 1588–1601. [CrossRef]
2. Lin, H. Study of Soft Rock Roadway Support Technique. *Procedia Eng.* **2011**, *26*, 321–326. [CrossRef]
3. Xu, Y.L.; Pan, K.R.; Zhang, H. Investigation of key techniques on floor roadway support under the impacts of superimposed mining: Theoretical analysis and field study. *Environ. Earth Sci.* **2019**, *78*, 436. [CrossRef]
4. Meng, Q.B.; Han, L.J.; Chen, Y.L.; Fan, J.D.; Wen, S.Y.; Yu, L.Y.; Li, H. Influence of dynamic pressure on deep underground soft rock roadway support and its application. *Int. J. Min. Sci. Technol.* **2016**, *26*, 903–912. [CrossRef]

5. Shi, P.; Qin, S.; Shui, Y.L.; Hu, P.P. Mechanism and control of end face roof fall accident in coal seam group mining. *Shaanxi Coal* **2022**, *41*, 121–125.
6. Chen, Y.; Bai, J.B.; Yan, S.; Hao, S.P.; Dao, V.D. A method for computing unsupported roof distance in roadway advancement and its in-situ application. *Int. J. Min. Sci. Technol.* **2016**, *26*, 551–556. [CrossRef]
7. Kang, H.P.; Jiang, P.F.; Yang, J.W.; Wang, Z.G.; Yang, J.H.; Liu, Q.B.; Wu, Y.Z.; Li, W.Z.; Gao, F.Q.; Jiang, Z.Y.; et al. Roadway soft coal control technology by means of grouting bolts with high pressure-shotcreting in synergy in more than 1000 m deep coal mines. *J. China Coal Soc.* **2021**, *46*, 747–762. [CrossRef]
8. Yang, S.W. Discussion on the design of temporary support structure of front detection beam in the side of coal roadway heading face. *Shanxi Chem. Ind.* **2022**, *42*, 153–155. [CrossRef]
9. Cui, X.Y. Application of ZLJ-10 Onboard Temporary Support Device in Yuxi Coal Mine. *Energy Energy Conserv.* **2021**, 168–169, 208. [CrossRef]
10. Du, J. The Mechanical Analysis and Optimization of Temporary Support Equipment Used in Arched Semi-Coal Rock Roadway. Master's Thesis, Liaoning Technical University, Fuxin, China, 2013.
11. Liu, Y.Y.; Xu, X.; Xu, H.C. The Design of Fast Roadway Drivage Support Work Platform. *Appl. Mech. Mater.* **2014**, *556*, 1116–1118. [CrossRef]
12. Cai, L.; Meng, F.L.; Li, S.C.; Guo, W.Y. Temporary Support Technology of Roadheader. *Coal Mine Mach.* **2013**, *34*, 189–191. [CrossRef]
13. Li, J.F.; Liu, B. Development of Temporary Hydraulic-pressure Canopy Guard for Full-mechanized Roadheader. *Coal Min. Technol.* **2010**, *15*, 73–74, 82. [CrossRef]
14. Jian, B. Research and application of digging machine's loaded-hydraulic-pressure provisional shoring. *Coal Tehcnol.* **2007**, *26*, 9–10.
15. Wang, S.W.; Wang, Y.; Zhao, C.L.; Wu, H. Design and Study of Roadheader-mounted Provisional Shoring Machine. *Coal Mine Mach.* **2011**, *32*, 52–53. [CrossRef]
16. Li, J.F. Development of Airborne Temporary Support Device for EBZ160 Tunnel Boring Machine. *Rock Drill. Mach. Pneum. Tools* **2014**, 53–54.
17. Yan, X.S.; Du, H.Y. Modification and application on on-board temporary support of roadheader. *Shaanxi Coal* **2017**, *36*, 82, 120–121.
18. Xin, Z.Y. Design and Application of Interlocking Shoring Mechanism Based on EBZ160 Roadheader Airborne Temporary Support. *Inn. Mong. Coal Econ.* **2019**, 94–95. [CrossRef]
19. Yang, C.X. Research on Inchworm Coal Mine Roadway Temporary Support. Master's Thesis, Liaoning Technical University, Fuxin, China, 2014.
20. Wang, L.L. Research of Hydraulic Support for Roadway Forepoling. Master's Thesis, Hebei University of Engineering, Handan, China, 2014.
21. Yang, D.H.; Ning, Z.X.; Lv, Z.H.; Bai, X.T. Application and development on new type walking self-moving advance temporary powered support. *Coal Sci. Technol.* **2015**, *43*, 84, 112–115. [CrossRef]
22. Yao, L.H.; Yang, D.H.; Ning, Z.X.; Lv, Z.H. Application and development on self-moving temporary support device for machine gateway. *Coal Sci. Technol.* **2016**, *44*, 150–154. [CrossRef]
23. Liu, Y.Z. Research on the Structure and Performance of the Self-Propelled Support Equipment Accompanying Road Header of Comprehensive Roadway. Master's Thesis, Liaoning Technical University, Fuxin, China, 2019.
24. Li, Y.H.; Li, Q.A.; Xie, X.C. Fast tunnelling Technology of Roadway Based on Tunnel-anchoring Machine. *Datong Coal Sci. Technol.* **2019**, 27–29. [CrossRef]
25. LI, Z.Q.; Wang, S.P.; Li, B.L. The present situation and development of supporting equipment in tunneling. *Coal Sci. Technol.* **1997**, 41–44. [CrossRef]
26. Wang, G. Research and Application of Rapid Excavation Technology of AIO Anchor Protecting Machine. *Shandong Coal Sci. Technol.* **2018**, 42–43. [CrossRef]
27. Palani, S.; Shanmugan, S.; Selvam, M.; Harisha, K.A. Stability analysis of self-propelled aerial man lift vehicles. *Int. J. Veh. Struct. Syst.* **2017**, *9*, 276–279. [CrossRef]
28. Chen, C.; Qin, D.L.; Ren, X.Q.; Ouyang, Y.W. Finite element analysis of the cylindrical rivet used in flat clinch-rivet process. *J. Braz. Soc. Mech. Sci. Eng.* **2021**, *43*, 577. [CrossRef]
29. Ren, J.P. The Research of the Structure of Self-Motion Assistance Powered Support Equipment for Roadway. Master's Thesis, Liaoning Technical University, Fuxin, China, 2009.
30. Lu, J.W. Parametric of Roadway Temporary Support and Part Optimization Design. Master's Thesis, Liaoning Technical University, Fuxin, China, 2012.
31. Zhang, P.C. Research on Key Technology and Equipment for Advanced Support Used in the Ends of Fully Mechanized Mine Face. Ph.D. Thesis, China University of Mining & Technology (Beijing), Beijing, China, 2013.
32. Li, N. The Research on Structure and Key Technology of Temporary Support Equipment Used in Rectangular Roadway. Master's Thesis, Liaoning Technical University, Fuxin, China, 2013.
33. Ma, Z.M. Self-Motion Temporary Support Structure Design and Mechanics Performance Research. Master's Thesis, Liaoning Technical University, Fuxin, China, 2014.

34. Yan, G.L. Optimal Analysis on Top Beam of Temporary Support Structure in the Coal Mine. *Mech. Manag. Dev.* **2020**, *35*, 114–116. [CrossRef]
35. Li, Y.G. Optimization Design of Temporary Support Equipment for Coal Mine Roadway Development. *Mech. Manag. Dev.* **2021**, *36*, 37–38, 41. [CrossRef]
36. Xie, G.X.; Chang, J.C.; Yang, K. Investigations into stress shell characteristics of surrounding rock in fully mechanized top-coal caving face. *Int. J. Rock Mech. Min. Sci.* **2009**, *46*, 172–181. [CrossRef]
37. Tian, Y. Research on Rock Mechanics of Temporary Support in the Initial Period of Tunnel Excavation. *Coal Mine Mod.* **2015**, 68–72. [CrossRef]
38. Yang, C.X.; Ding, L.; Tang, D.W.; Gao, H.B.; Deng, Z.Q. Improved Terzaghi-theory-based interaction modeling of rotary robotic locomotors with granular substrates. *Mech. Mach. Theory* **2020**, *152*, 103901. [CrossRef]
39. Xie, S.; Zhou, H. Numerical Simulation on Lining Support of Tunnel Based on Terzaghi Theory. *Min. Res. Dev.* **2016**, *5*, 90–93. [CrossRef]
40. Wang, G.F.; Pang, Y.H. Relationship between hydraulic support and surrounding rock coupling and its application. *J. China Coal Soc.* **2015**, *40*, 30–34. [CrossRef]
41. Yang, Y.; Ma, Q.Q. Research and application of support technology in tunneling. *Energy Technol. Manag.* **2020**, *35*, 83–85. [CrossRef]
42. Choi, S.O.; Shin, H.S. Stability analysis of a tunnel excavated in a weak rock mass and the optimal supporting system design. *Int. J. Rock Mech. Min. Sci.* **2004**, *41*, 876–881. [CrossRef]
43. Chen, W.H.; Uribe, M.C.; Kwon, E.E.; Lin, K.A.; Park, Y.K.; Ding, L.; Saw, L.H. A comprehensive review of thermoelectric generation optimization by statistical approach: Taguchi method, analysis of variance (ANOVA), and response surface methodology (RSM). *Renew. Sustain. Energy Rev.* **2022**, *169*, 112917. [CrossRef]
44. Manojkumar, N.; Muthukumaran, C.; Sharmila, G. A comprehensive review on the application of response surface methodology for optimization of biodiesel production using different oil sources. *J. King Saud Univ. Eng. Sci.* **2022**, *34*, 198–208. [CrossRef]
45. Ibrahim, I.; James, B.B.; Musa, N.D.; Ayodeji, N.O.; Kazeem, A.S.; Elijah, O.O. Response surface methodology for the optimization of the effect of fibre parameters on the physical and mechanical properties of deleb palm fibre reinforced epoxy composites. *Sci. Afr.* **2022**, *16*, e01269. [CrossRef]
46. Wu, J.J.; Wang, Z.N.; Ren, C.X.; Xin, M.Y. Lightweight Design for Lift Drum Line Bracket Based on Response Surface Method. *Mach. Des. Manuf.* **2020**, 263–266. [CrossRef]
47. Deb, K.; Agrawal, S.; Pratap, A.; Meyarivan, T. A fast and elitist multio bjective genetic algorithm: NSGA-II. *IEEE Trans. Evol. Comput.* **2002**, *6*, 182–197. [CrossRef]
48. Hussain, M.; Wei, L.F.; Abbas, F.; Rehman, A.; Ali, M.; Lakhan, A. A multi-objective quantum-inspired genetic algorithm for workflow healthcare application scheduling with hard and soft deadline constraints in hybrid clouds. *Appl. Soft Comput.* **2022**, *128*, 109440. [CrossRef]